
Article:
Fathi, F., Chen, L. and de Borst, R. (2020) Extended isogeometric analysis for cohesive fracture. International Journal for Numerical Methods in Engineering, 121 (10). pp. 4584-4613. ISSN 0029-5981

https://doi.org/10.1002/nme.6453

Received: Added at production | Revised: Added at production | Accepted: Added at production

DOI: xxx/xxxx

ARTICLE TYPE

Extended isogeometric analysis for cohesive fracture

Farshid Fathi | Lin Chen | René de Borst*

Department of Civil and Structural Engineering, University of Sheffield, Sheffield, UK

Correspondence
*Department of Civil and Structural Engineering, University of Sheffield, Sheffield, S1 3JD, UK
Email: r.deborst@sheffield.ac.uk

ABSTRACT

The objective of this study is to present an eXtended IsoGeometric formulation for cohesive fracture. The approach exploits the higher-order inter-element continuity property of Non-Uniform Rational B-Splines (NURBS), in particular the higher accuracy that results for the stress prediction, which yields an improved estimate for the direction of crack propagation compared to customary Lagrangian interpolations. Shifting is used to ensure compatibility with the surrounding discretisation, where, different from eXtended Finite Element Methods, the affected elements stretch over several rows perpendicular to the crack path. To avoid fine meshes around the crack tip in case of cohesive fracture, a blending function is used in the extension direction of the crack path. To comply with standard finite element data structures Bézier extraction is used. The absence of the Kronecker-delta property in the higher-order interpolations of Isogeometric Analysis impedes the enrichment scheme and compatibility enforcement. These issues are studied comprehensively at the hand of several examples, while crack propagation analyses show the viability of the approach.

KEYWORDS:
Isogeometric analysis, cohesive fracture, Bézier extraction, extended finite element analysis, compatibility enforcement

1 | INTRODUCTION

Fracture is an important topic of study in the mechanics of solids and a good understanding is pivotal for the proper assessment of structural integrity. Fracture mechanics encompasses a wide spectrum of experimental and theoretical studies, and involves different physical phenomena. The fracture process zone, a limited zone in front of the crack tip where inelastic deformations take place, is an important concept, which is central in deciding which modelling approach should be adopted. When the size of the fracture process zone is small compared to a typical structural dimension, Linear Elastic Fracture Mechanics[1,2] is the method of choice. However, when the fracture process zone becomes non-negligible, cohesive-zone models[3,4,5] are often more applicable from a physics point of view. This holds, for instance, for many problems in fractured, fluid-saturated porous media[6].

The incorporation of a displacement discontinuity like a crack, into a continuum mechanics framework can basically be accomplished in two different ways: either the discontinuity is captured rigorously and additional degrees of freedom are created, or the discontinuity is embedded in an element, and the displacement discontinuity is transformed into an additional, incompatible, Dirac-delta like strain mode inside an element[7], and different variants of this approach have been put forward. The downside of the latter approach, however, is that the discontinuity is not directly resolved. Moreover, although the approach mitigates the notorious mesh sensitivity issue in strain softening solids, the underlying issue of a loss of well -posedness of the boundary value problem is not solved[8].

Interface elements are the conventional way to capture a (potential) crack as an inter-element discontinuity which fully preserves the discontinuous crack[9,10,11]. They are simple to implement and robust in terms of computational performance. Yet, the approach suffers from the need to know the crack direction beforehand. Re-meshing is an obvious remedy and has been applied successfully, including in cohesive fracture[12,13,14].

In a different approach, an arbitrarily shaped discontinuity can be inserted by adding an additional set of discontinuous functions with own degrees of freedom to the regular displacement field by exploiting the partition of unity property of finite element basis functions. This method has been coined the eXtended Finite Element Method (XFEM) and can be considered as a generalisation of interface elements, as these elements are retrieved as the limiting case of XFEM when the discontinuity is put at the edge of an element. Yet, some major differences exist. First, crack propagation can be entirely arbitrary, free of the underlying, original mesh lay-out. Secondly, the dummy stiffness, which is needed in interface elements to keep the discontinuity closed prior to local crack initiation, is not needed in XFEM because locally new degrees of freedom are created only when the crack has propagated to this point,[8,15,16]. While the eXtended Finite Element Method was originally proposed in conjunction with Linear Elastic Fracture Mechanics[17,18], applications of XFEM to cohesive-zone models have also been proposed[19,20].

The latter contributions were also the first to utilise a higher-order XFEM for both the regular and the extended parts. Six-noded triangular elements were employed, even though the crack was still conceived as a set of straight discontinuities approximated with lines, which restriction was dropped by Stazi *et al.*[21], who used a quadratic discretisation for the regular part and for approximating the geometry of the curved crack, while the interpolation of the extended part remained linear. A convergence study for higher-order extended finite element methods[22] showed that the same polynomial order has to be utilised in the standard as well as in the extended part in order to resolve the displacement field properly.

IsoGeometric Analysis (IGA) was proposed with the aim to have the same set of basis functions for the design process and for the analysis[23]. Aside from capturing the geometry exactly, the method has the major advantage that it provides a higher-order inter-element continuity, enabling, for instance, to have a continuous stress field across element boundaries. The enhanced accuracy in stress prediction is particularly important in the vicinity of crack tips, where traditional Lagrange basis functions usually perform rather poorly. This is most relevant for free crack propagation, where the direction of crack extension is fully governed by the accuracy of the local stress field.

An eXtended IsoGeometric Analysis method (XIGA) was first proposed by De Luycker *et al.*[24] for Linear Elastic Fracture Mechanics. Two types of interpolation were investigated: the same order of interpolation for both parts, and a higher-order interpolation for the standard part combined with a linear interpolation for the extended part. Different from XFEM, eXtended IsoGeometric Analysis cannot handle a linear interpolation in the extended part when the standard part has a higher-order interpolation[24]. Moreover, a conflict in the blending element where the tip and the Heaviside enrichments coincide, has been observed. As a remedy, C^0-lines have been suggested for the standard as well as the extended part, such that Non-Uniform Rational B-splines (NURBS) reduce to Lagrange basis functions, or in other words, XIGA coincides with XFEM. As an alternative remedy, a least square technique was utilised in the weight (blending) functions for the tip and Heaviside enrichments. Convergence rates for the case of the same polynomial orders in the standard and extended parts have been reported by De Luycker *et al.*[24] and Ghorashi *et al.*[25].

Herein, we propose an eXtended IsoGeometric Analysis formulation for cohesive fracture. To enforce compatibility in the direction perpendicular to the crack path we will use a shifting technique. The use of shifting in isogeometric analysis is more complicated than in standard finite element analysis, as, due to the higher-order continuity, the area in which compatibility has to be enforced is several rows of elements wide instead of a single row. Another issue is the fact that the Kronecker delta property does not hold when using B-splines or Non-Uniform Rational B-Splines (NURBS), the basis functions in isogeometric analysis. In the direction of the crack, i.e. ahead of the crack tip, a blending technique has been used to avoid the required very fine meshes ahead of the crack tip, which is particularly relevant for cohesive fracture. Finally, to achieve compatibility with standard finite element data structures, Bézier extraction has been used similar to an XIGA application in Linear Elastic Fracture Mechanics[26]. Rate-independent, isotropic linear elasticity has been used for the bulk material, while the displacement gradients are assumed to be small throughout.

This contribution starts with a succinct discussion of the cohesive-zone approach, including a discussion how to extend the crack. The strong and weak forms of the governing equations are stated to set the scene for the ensuing discussion on a Bézier extraction based eXtended IsoGeometric Analysis method. Aspects of compatibility and implemenation are covered as well. Next is an assessment of the properties of the approach, including the effect of the order of the interpolation, and the order of the continuity. The paper concludes with case studies of a plate with a circular void, and crack propagation along straight and curved paths.

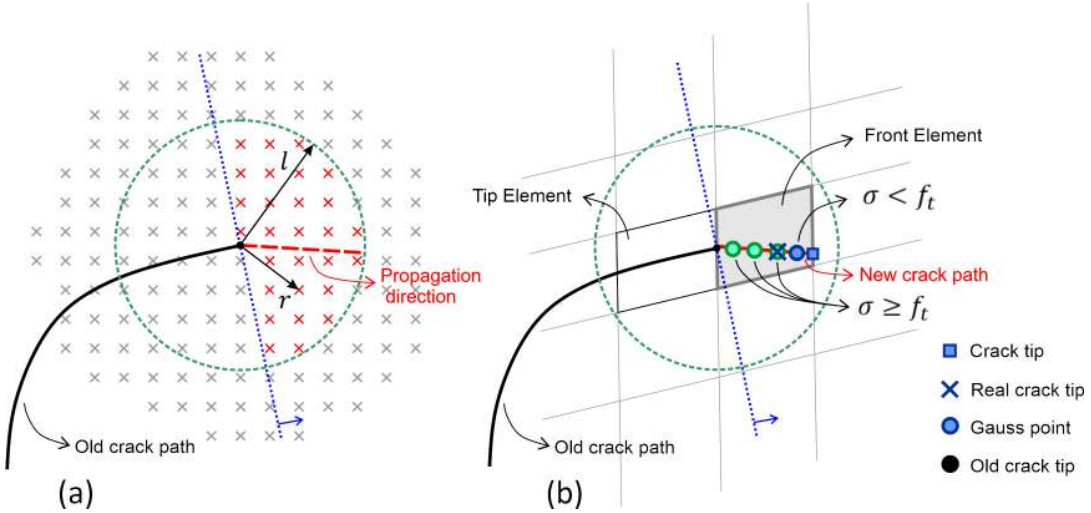

FIGURE 1 Non-local calculation of the crack propagation direction. The blue arrow illustrates the direction of the crack tip front. In (a), the green dashed circle determines which Gauss points are considered for non-local computation, while red marks are Gauss points used in the computation of the non-local stress. In (b), the crack tip and real crack tip are defined, which is determined by comparing the principal stress σ with the fracture strength f_t.

2 | COHESIVE-ZONE MODEL

In this contribution we adopt the cohesive crack concept, in which the inelastic deformations in the fracture process zone are thought to be concentrated in a line. Tractions act across this discontinuity which are a function of the local crack opening.

2.1 | Traction-separation relation

Herein, we assume that the relation between the normal traction and the crack opening follows an exponential curve:

$$t_n = f_{\mathrm{t}} \exp\left(-\frac{f_{\mathrm{t}}}{G_{\mathrm{f}}}\kappa\right) \tag{1}$$

where f_{t} and G_{f} are the tensile strength and the fracture energy, respectively, and κ is a history parameter equal to the largest value attained till the current loading step. The loading/unloading condition is based on a loading function

$$f\left(\llbracket u_n \rrbracket, \kappa\right) = \llbracket u_n \rrbracket - \kappa \tag{2}$$

such that $f \geq 0$ denotes loading, while $f < 0$ indicates unloading.

In order to obtain a symmetric tangent, the crack shear stiffness is assumed to be zero. To obtain the linearised tangent in the local coordinates, Equation (2) is differentiated with respect to time:

$$\left\{ \begin{array}{c} \dot{t}_s \\ \dot{t}_n \end{array} \right\} = \underbrace{\left[\begin{array}{cc} 0 & 0 \\ 0 & -\frac{f_{\mathrm{t}}^2}{G_{\mathrm{f}}} \exp\left(-\frac{f_{\mathrm{t}}}{G_{\mathrm{f}}}\kappa\right) \end{array} \right]}_{\mathbf{T}_d} \left\{ \begin{array}{c} \llbracket \dot{u}_s \rrbracket \\ \llbracket \dot{u}_n \rrbracket \end{array} \right\} \tag{3}$$

A secant stiffness is assumed for unloading.

2.2 | Direction of the extension of the discontinuity

Even though isogeometric analysis vastly improves the stress prediction around the crack tip for B-splines, the direction of crack propagation can be highly influenced by small accuracies in the principal stresses, which determine the crack extension. Therefore, we adopt a non-local approximation of the stresses around the crack tip earlier considered in eXtended Finite Element

analysis[19]. We emphasise that only Gauss points in front of the crack tip are considered, i.e. the red-coloured Gauss points in Figure 1. The Gaussian distribution function is used as the weighting function for the non-local approximation[27]:

$$w = \frac{1}{(2\pi)^{3/2} l^3} \exp\left(-\frac{r^2}{2l^2}\right) \tag{4}$$

where r and l are the distance vector of each Gauss point and a length parameter, respectively, see Figure 1. The length parameter is typically taken 2-3 times the length of a diagonal of a typical element[19]. Calculating the non-local stress components for the crack tip, we can locate the new crack propagation direction based on the principal stresses (dashed red line in Figure 1). After determining the crack direction, the end point of the crack can be located, since the crack is assumed as a straight line passing throughout the element.

3 | GOVERNING EQUATIONS

We now briefly discuss the kinematics of a discontinuity within a continuum formulation. The enhanced displacement field is defined, including the calculation of the displacement at the discontinuity. Next, the discontinuous displacement fields and a traction-separation relation are defined and the weak forms are derived. The latter are the starting point for the discretisation in an isogeometric framework.

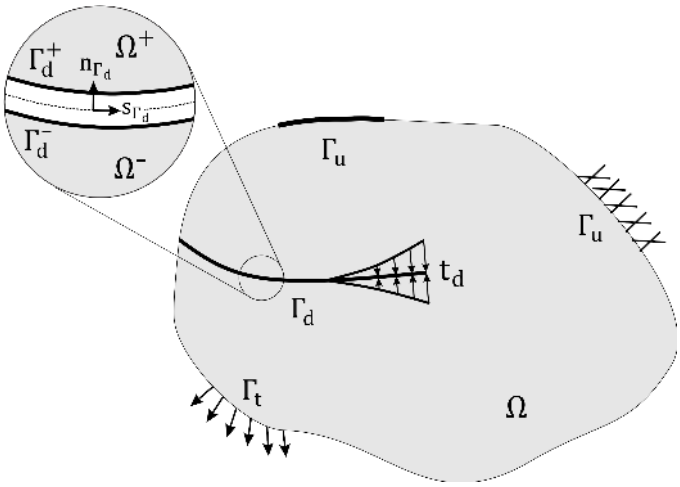

FIGURE 2 Body Ω with a discontinuity Γ_d.

3.1 | Kinematics of the displacement discontinuity and constitutive equilibrium equation

The partition of unity property holds for Lagrange interpolation functions, typically used within standard finite element methods, as well as for B-splines and NURBS, which are the prototypical interpolation functions used in isogeometric analysis. Exploiting this property the total displacement field can be written as the sum of two sub-fields, as follows:

$$u(\mathbf{x}) = \sum_{i=1}^{n} \phi_i(\mathbf{x}) \left(a_i + \sum_{j=1}^{m} b_{ij} \gamma_j(\mathbf{x}) \right) \tag{5}$$

In Equation (5), ϕ_i are the regular basis functions, γ_j is an enhanced basis with m terms, a_i and b_{ij} are the regular and the enhanced nodal degrees of freedom, respectively. For our purpose a single additional term suffices, so that $m = 1$. However, cases with $m > 1$ have been reported[28,29] for different reasons, including robust conditioning or an improved convergence rate. In standard finite element methods, the enhanced basis is empty, unlike in eXtended or Generalised Finite Element methods (GFEM or XFEM) in order to improve the approximation. Employing a standard finite element notation for an n-noded element

with one enriched term, Equation (5) can be written in matrix-vector form as:

$$\mathbf{u}(\mathbf{x}) = \mathbf{N}(\mathbf{x})\mathbf{a} + \tilde{\mathbf{N}}(\mathbf{x})\mathbf{N}_{\gamma}(\mathbf{x})\mathbf{H}\mathbf{b} \tag{6}$$

where $\mathbf{N}$ contains the standard finite element shape functions and $\mathbf{N}_{\gamma}$ is the matrix which contains the enhancement, while $\mathbf{a}$ and $\mathbf{b}$ are the regular and enhanced degrees of freedom, respectively. To generalise the formulation, a different set of basis functions $\tilde{\mathbf{N}}$ has been used in the extended part. $\mathbf{H}$ is a diagonal matrix to include or remove enriched nodes by switching the corresponding diagonal entries between 0 and 1, so that Equation (6) implies a bijective relation between the standard and enhanced degrees of freedom for each node which enables activation or deactivation of the enriched part[30]. This feature provides a conventional finite element displacement field with a customised local enrichment. We consider the body of Figure 2. While the regular degrees of freedom represent the continuous displacement field, the enhanced degrees of freedom can represent a discontinuity when:

$$\mathbf{u}(\mathbf{x}) = \mathbf{N}(\mathbf{x})\mathbf{a} + \mathcal{H}_{\Gamma_d}(\mathbf{x})\tilde{\mathbf{N}}(\mathbf{x})\mathbf{b} \tag{7}$$

The choice for the (discontinuous) enrichment function differs depending on the physics of discontinuity. Herein, a crack is considered, which is modelled as a strong discontinuity, but weak discontinuities can be modelled as well[31,15].

As not uncommon in eXtended Finite Element methods, we have adopted level sets for tracking the crack as a moving interface. A zero level set denotes the interface itself and higher levels represent the propagation of the interface. This eliminates the necessity to explicitly define the interface geometry. The most common level set function is the signed distance defining the position of an arbitrary point with respect to the interface, see Figure 3[15]:

$$\varphi(\mathbf{x}) = \|\mathbf{x} - \mathbf{x}^*\| \ \text{sign}\left(\mathbf{n}_{\Gamma_d} \cdot (\mathbf{x} - \mathbf{x}^*)\right) \tag{8}$$

where $\|\cdot\|$ denotes the Euclidean norm, $\mathbf{x}^*$ is the closest projection of point $\mathbf{x}$ onto the interface, and $\mathbf{n}_{\Gamma_d}$ is the normal vector at point $\mathbf{x}^*$ on the interface. Based on Equation (8), the level set function divides the domain into three zones:

$$\varphi(\mathbf{x}) = \begin{cases} < 0 \ \text{if} \ \mathbf{x} \in \Omega^- \\ = 0 \ \text{if} \ \ \mathbf{x} \in \Gamma_d \\ > 0 \ \text{if} \ \mathbf{x} \in \Omega^+ \end{cases} \tag{9}$$

The Heaviside function adopted in this paper is defined as:

$$\mathcal{H}_{\Gamma_d}(\mathbf{x}) = \text{sign}(\varphi(\mathbf{x})) = \begin{cases} -1 \ \text{if} \ \varphi(\mathbf{x}) < 0 \\ 0 \quad \text{if} \ \varphi(\mathbf{x}) = 0 \\ +1 \ \text{if} \ \varphi(\mathbf{x}) > 0 \end{cases} \tag{10}$$

Recalling the small strain assumption, the strain field can be calculated by taking the gradient of Equation (7):

$$\boldsymbol{\epsilon} = \mathbf{B}\mathbf{a} + \mathcal{H}_{\Gamma_d}\tilde{\mathbf{B}}\mathbf{b} + 2\left(\delta_{\Gamma_d}\mathbb{n}_{\Gamma_d}\right)\tilde{\mathbf{N}}\mathbf{b} \tag{11}$$

where $\tilde{\mathbf{B}}$ is the matrix of derivatives corresponding to the set of basis functions $\tilde{\mathbf{N}}$ in the extended part. δ_{Γ_d} is the Dirac-delta function and $\mathbb{n}_{\Gamma_d}$ is the matrix containing the components of the normal vector to the discontinuity:

$$\mathbb{n}_{\Gamma_d}^{\mathrm{T}} = \begin{bmatrix} (n_{\Gamma_d})_x & 0 & (n_{\Gamma_d})_y \\ 0 & (n_{\Gamma_d})_y & (n_{\Gamma_d})_x \end{bmatrix} \tag{12}$$

In the absence of the acceleration and body forces, the equilibrium equation reads:

$$\begin{cases} \nabla \cdot \boldsymbol{\sigma} = 0 & \mathbf{x} \in \Omega \\ \mathbf{u} = \overline{\mathbf{u}} & \mathbf{x} \in \Gamma_u \\ \mathbf{n} \cdot \boldsymbol{\sigma} = \overline{\mathbf{t}} & \mathbf{x} \in \Gamma_t \\ \mathbf{n}_{\Gamma_d} \cdot \boldsymbol{\sigma} = \mathbf{t}_d & \mathbf{x} \in \Gamma_d \end{cases} . \tag{13}$$

where $\boldsymbol{\sigma}$ is the Cauchy stress tensor, $\mathbf{n}$ is the normal vector to the external traction surface and $\mathbf{n}_{\Gamma_d}$ is the vector normal to the crack surface, see Figure 2. The prescribed displacement and traction are defined as $\overline{\mathbf{u}}$ and $\overline{\mathbf{t}}$, respectively. The stress-strain relation for the bulk material is assumed to be linear-elastic:

$$\boldsymbol{\sigma} = \mathbf{D} : \boldsymbol{\epsilon} \tag{14}$$

where $\mathbf{D}$ is the fourth-order linear-elastic stiffness tensor. In a similar fashion, the traction in a local coordinate system is a function of the crack opening as:

$$\mathbf{t}_d^{\text{loc}} = \mathbf{t}_d^{\text{loc}} \left([\![\mathbf{u}_d]\!] \right) \tag{15}$$

where $[\![\mathbf{u}_d]\!]$ is the displacement jump at the discontinuity. For use within a Newton-Raphson type iterative scheme this relation must be linearised, leading to

$$\dot{\mathbf{t}}_d^{\text{loc}} = \mathbf{T}_d \cdot [\![\dot{\mathbf{u}}_d^{\text{loc}}]\!] \tag{16}$$

where $\mathbf{T}_d$ has already been defined in Equation (3). Using the rotation tensor $\mathbf{Q}$ between the local and the global coordinate systems, this relation can be modified as:

$$\dot{\mathbf{t}}_d = \mathbf{Q}^{\text{T}} \cdot \mathbf{T}_d \cdot \mathbf{Q} [\![\dot{\mathbf{u}}_d]\!] \tag{17}$$

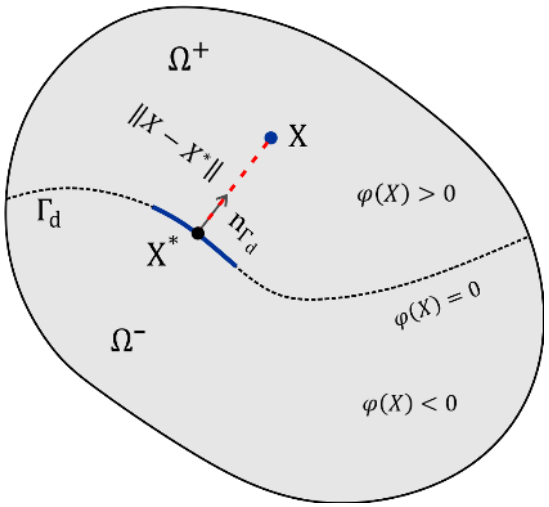

FIGURE 3 Determination of the signed distance. The point $\mathbf{X}^*$ is the closest projection of the point $\mathbf{X}$ onto the discontinuity Γ_d

.

3.2 | Variational formulation

To generalise the variational formulation, η ($\hat{\eta}$ for the standard and $\tilde{\eta}$ for the extended part) is used to cover all admissible variables, including u. Employing the principle of virtual work, the equilibrium equation from (13) can be written in a weak form:

$$\int_{\Omega} \nabla^{\text{s}} \boldsymbol{\eta} \, : \, \boldsymbol{\sigma} \, \text{d}\Omega - \int_{\Gamma_u} \boldsymbol{\eta} \cdot \bar{\mathbf{t}} \, \text{d}\Gamma = 0 \tag{18}$$

which must hold for all admissible variations, and where in line with Equation (7), the variations of the displacement are decomposed into the regular displacement $\hat{\eta}$ and the displacement jump $\tilde{\eta}$ as [19]:

$$\boldsymbol{\eta} = \hat{\boldsymbol{\eta}} + \mathcal{H}_{\Gamma_d} \tilde{\boldsymbol{\eta}} \tag{19}$$

Inserting Equation (19) into Equation (18) yields:

$$\int_{\Omega} \nabla^{\text{s}} (\hat{\boldsymbol{\eta}} + \mathcal{H}_{\Gamma_d} \tilde{\boldsymbol{\eta}}) \, : \, \boldsymbol{\sigma} \, \text{d}\Omega = \int_{\Gamma_u} (\hat{\boldsymbol{\eta}} + \mathcal{H}_{\Gamma_d} \tilde{\boldsymbol{\eta}}) \cdot \bar{\mathbf{t}} \, \text{d}\Gamma \tag{20}$$

The gradient of the displacement field in Equation (20) reads:

$$\nabla^{\text{s}} \boldsymbol{\eta} = \nabla^{\text{s}} \hat{\boldsymbol{\eta}} + \mathcal{H}_{\Gamma_d} (\nabla^{\text{s}} \tilde{\boldsymbol{\eta}}) + 2 \delta_{\Gamma_d} (\tilde{\boldsymbol{\eta}} \otimes \mathbf{n}_{\Gamma_d})^{\text{s}} \tag{21}$$

Inserting Equation (21) into Equation(20) and using the identity $\int_\Omega \delta_{\Gamma_d}(\mathbf{x})\phi(\mathbf{x})d\Omega = \int_\Gamma \phi(\mathbf{x})d\Gamma$, leads to the following weak form:

$$\int_\Omega \nabla^s\hat{\boldsymbol{\eta}} : \boldsymbol{\sigma}\mathrm{d}\Omega + \int_\Omega \mathcal{H}_{\Gamma_d}(\nabla^s\tilde{\boldsymbol{\eta}}) : \boldsymbol{\sigma}\mathrm{d}\Omega + 2\int_{\Gamma_d} \left(\tilde{\boldsymbol{\eta}} \otimes \mathbf{n}_{\Gamma_d}\right)^s : \boldsymbol{\sigma}\mathrm{d}\Gamma = \int_{\Gamma_u} (\hat{\boldsymbol{\eta}} + \mathcal{H}_{\Gamma_d}\tilde{\boldsymbol{\eta}}) \cdot \bar{\mathbf{t}}\mathrm{d}\Gamma \tag{22}$$

where $\left(\tilde{\boldsymbol{\eta}} \otimes \mathbf{n}_{\Gamma_d}\right) : \boldsymbol{\sigma}$ can be rewritten as $\tilde{\boldsymbol{\eta}} \cdot \left(\boldsymbol{\sigma} \cdot \mathbf{n}_{\Gamma_d}\right)$, which yields:

$$\int_\Omega \nabla^s\hat{\boldsymbol{\eta}} : \boldsymbol{\sigma}\mathrm{d}\Omega + \int_\Omega \mathcal{H}_{\Gamma_d}(\nabla^s\tilde{\boldsymbol{\eta}}) : \boldsymbol{\sigma}\mathrm{d}\Omega + 2\int_{\Gamma_d} \tilde{\boldsymbol{\eta}} \cdot \mathbf{t}_d\mathrm{d}\Gamma = \int_{\Gamma_u} (\hat{\boldsymbol{\eta}} + \mathcal{H}_{\Gamma_d}\tilde{\boldsymbol{\eta}}) \cdot \bar{\mathbf{t}}\mathrm{d}\Gamma \tag{23}$$

which results in two separate variational equations for $\hat{\eta}$ and $\tilde{\eta}$:

$$\int_\Omega \nabla^s\hat{\boldsymbol{\eta}} : \boldsymbol{\sigma}\mathrm{d}\Omega = \int_{\Gamma_u} \hat{\boldsymbol{\eta}} \cdot \bar{\mathbf{t}}\mathrm{d}\Gamma \tag{24a}$$

$$\int_\Omega \mathcal{H}_{\Gamma_d}(\nabla^s\tilde{\boldsymbol{\eta}}) : \boldsymbol{\sigma}\mathrm{d}\Omega + 2\int_{\Gamma_d} \tilde{\boldsymbol{\eta}} \cdot \mathbf{t}_d\mathrm{d}\Gamma = \int_{\Gamma_u} \mathcal{H}_{\Gamma_d}\tilde{\boldsymbol{\eta}} \cdot \bar{\mathbf{t}}\mathrm{d}\Gamma. \tag{24b}$$

4 | EXTENDED ISOGEOMETRIC ANALYSIS

The possibility to control the inter-element continuity is the salient characteristic of B-splines and has been used to introduce discrete discontinuity by order reduction[32,13]. Alternatively, similar to the extended finite element method, B-splines can be enriched by a Heaviside function to introduce a discontinuity, since they also form a partition of unity, cf Equation (7). We will now succinctly review the main features of B-splines, and subsequently we employ them in an extended framework.

4.1 | Bézier extraction for NURBS

B-splines are the basis technology used in Computer-Aided Design, and were subsequently also used for analysis. Their higher-order inter-element continuity is highly advantageous for solving higher-order differential equations, which are frequently encountered in structural analysis[33].

A univariate B-spline is a piecewise polynomial represented with a monotonically increasing set of values, usually referred to as the knot vector, $\Xi = \left\{\xi_1, \xi_2, \cdots \xi_{n+p+1}\right\}$. n and p denote the number and the order of the knot vector, respectively. The customary choice of open knot vectors has followed here, where the multiplicity of the first and the last knot value are elevated to $p+1$. For simplicity, open knot vectors will be referred to as knot vectors in the remainder. The knot vector Ξ is constructed of m non-negative intervals representing the number of elements in the parameter domain. The geometry of a B-spline is also parametrised as a linear combination of basis functions N:

$$\mathbf{x}(\xi) = \mathbf{P}_k^{\mathrm{T}} N_k(\xi) \tag{25}$$

where $\mathbf{P}_k$ denotes the set of control points in the physical domain, and $N_k(\xi)$ maps a coordinate ξ from the parameter domain onto the physical domain. The B-spline basis functions are recursively defined by the Cox-de Boor formula[8]:

$$N_{k,p}(\xi) = \frac{\xi - \xi_k}{\xi_{k+p} - \xi_k} N_{k,p-1}(\xi) + \frac{\xi_{k+p+1} - \xi}{\xi_{k+p+1} - \xi_{k+1}} N_{k+1,p-1}(\xi) \tag{26}$$

with the initial value for zeroth order ($p = 0$):

$$N_{k,0}(\xi) = \begin{cases} 1 & \xi_k \le \xi < \xi_{k+1} \\ 0 & \text{otherwise.} \end{cases} \tag{27}$$

B-splines were replaced by Non-Uniform B-Splines (NURBS) in Computer-Aided Design owing to their ability to accurately parametrise conic shapes[8]. A NURBS basis function R is defined as a weighted B-spline basis function N,

$$R_{k,p}(\xi) = \frac{w_k N_{k,p}}{W(\xi)}. \tag{28}$$

with $N_{k,p}$ defined in Equations (26), w_k is the weight of the corresponding knot, and $W(\xi) = \sum_{k=1}^{n} N_k(\xi) w_k$ is the weighting function. A NURBS curve can be extended to a NURBS surface

$$\mathbf{S}(\xi,\eta) = \sum_{k=1}^{n}\sum_{l=1}^{m} R_{k,l}^{p,q}(\xi,\eta)\mathbf{p}_{k,l} \tag{29}$$

with the bivariate NURBS basis function defined as the tensor product of univariate bases[34]:

$$R_{k,l}^{p,q}(\xi,\eta) = \frac{M_{l,q}(\eta)N_{k,p}(\xi)w_{k,l}}{\sum_{\hat{k}}^{n}\sum_{\hat{l}}^{m} M_{\hat{k},q}(\eta)N_{\hat{l},p}(\xi)w_{\hat{k},\hat{l}}}. \tag{30}$$

To provide an element-wise framework for B-splines and NURBS, similar to standard finite elements, Bézier extraction has been proposed[34,35]. A degree p Bézier curve can be defined as a linear combination of Bernstein polynomial basis functions and a set of control points[34]. The Bernstein polynomials can be recursively defined over [-1 1]. These polynomials were originally defined for $\xi \in [0\ 1]$, while have been redefined on [-1 1] to facilitate the integration[34]:

$$B_{k,p}(\xi) = \frac{1}{2}(1-\xi)B_{k,p-1}(\xi) + \frac{1}{2}(1+\xi)B_{k-1,p-1}(\xi) \tag{31}$$

where

$$B_{1,0}(\xi) \equiv 1 \tag{32}$$

and

$$B_{k,p}(\xi) \equiv 0 \quad \text{if } k < 1 \text{ or } k > p+1. \tag{33}$$

A combination of the chain rule and the tensor product results in bivariate basis functions of Bernstein polynomials. Derivatives of Bernstein basis functions are given in Appendix A.

$$B_{k,l}^{p,q}(\xi,\eta) = B_{k,p}(\xi) \otimes B_{l,q}(\eta). \tag{34}$$

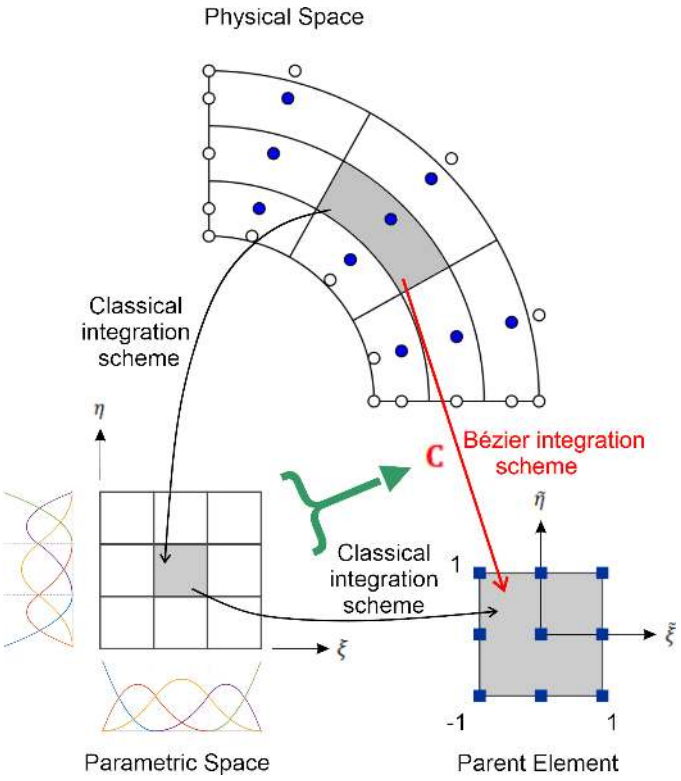

FIGURE 4 Comparison between classical integration and a Bézier-extraction based integration scheme, where C is the Bézier extraction operator

.

Using knot insertion, i.e. increasing the multiplicity of knot values and consequently decreasing the order of the continuity without changing geometric and parametric properties of the curve[34], Bézier elements of the curve can be generated. In this process, the multiplicity of each interior knot is increased to the order of the knot vector p to obtain C^0-continuity at the boundaries of the elements. A detailed description of Bézier extraction has been given by Borden *et al.*[34], while it has been extended to Bézier interface elements by Irzal *et al.*[10]. The element-specific B-spline basis functions can be constructed as a linear combination of a canonical set of polynomial basis function, $\boldsymbol{\mathcal{B}}$:

$$\mathbf{N}^e = \mathbf{C}^e \boldsymbol{\mathcal{B}} \tag{35}$$

with $\mathbf{C}^e$ the transformation matrix which is also referred as Bézier extraction operator. $\boldsymbol{\mathcal{B}}$ contains the Bernstein basis functions. From an implementation perspective Bézier extraction does not affect the model-specific process since it only modifies the basis function[34]. Therefore, the same B-spline bases can be used for the model. Furthermore, by calculating the Bézier extraction operator, there is no need to construct the parametric domain explicitly. This facilitates the integration process since the physical domain can be directly mapped to the parent element similar to the traditional finite element, while classical process necessitates two mappings, Figure 4.

Since the only difference between B-splines and NURBS is the weight used in the latter, the first step towards a Bézier element based NURBS formulation is the redefinition of the weight function in Equation (28)[34,35]:

$$W(\xi) = \sum_{k=1}^{n} N_k(\xi) w_k = \mathbf{w}^{\mathrm{T}} \mathbf{N}(\xi) = \mathbf{w}^{\mathrm{T}} \mathbf{C} \boldsymbol{\mathcal{B}}(\xi) = \left(\mathbf{C}^{\mathrm{T}} \mathbf{w}\right)^{\mathrm{T}} \boldsymbol{\mathcal{B}}(\xi) = \left(\mathbf{w}^b\right)^{\mathrm{T}} \boldsymbol{\mathcal{B}}(\xi) = W^b(\xi) \tag{36}$$

Substitution of Equations (35) and (36) into Equation (28) then gives the NURBS basis function:

$$\mathbf{R}^e(\xi) = \mathbf{W}^e \frac{\mathbf{N}^e(\xi)}{W^e(\xi)} = \mathbf{W}^{be} \mathbf{C}^e \frac{\boldsymbol{\mathcal{B}}^e(\xi)}{W^{be}(\xi)} \tag{37}$$

with $\mathbf{w}$ the vector associated with the weights in the diagonal matrix of weights, $\mathbf{w} = \{w_k\}_{k=1}^{n}$. Thus, in the same manner $\mathbf{w}^b = \{w_k^b\}_{k=1}^{n+m}$, and $\mathbf{W}^b$ is the corresponding diagonal matrix of weights. The element-wise derivatives of NURBS basis function are given in Appendix A.

4.2 | Compatibility enforcement

Numerous contributions have been devoted on how to enforce compatibility of the standard and the enhanced displacement fields in the in extended finite element method. Enforcing compatibility in extended isogeometric analysis, however, is a challenge which has hardly been addressed. Nevertheless, the issue is even more pressing, and complicated, due to the very reason that isogemetric analysis can enhance the order of continuity at element boundaries. De Luycker *et al.*[24] have studied the limitations and the difficulties of the *blending* technique in a comprehensive manner, but have mentioned another possible technique to enforce compatibility, namely *shifting*, only in passing. Herein, we will describe the shifting technique for higher-order interpolations, see Figure 5c for a definition. Figure 5 illustrates the effect of the Bézier extraction operator on the Bernstein basis functions containing the discontinuity with shifting.

Remark 1: In this manuscript, the notion order of continuity relates to the element boundaries, unless mentioned otherwise. For example, C^0 element denotes all interpolations with C^0-continuity at element boundaries, e.g. quadratic^0 means a quadratic element with C^1 non-zero continuity inside the element and C^0-continuity at element boundaries.

Remark 2: B-splines generally do not provide the Kronecker-delta property. However, similar to open knot vectors, Bézier B-spline elements partially provide this property at element boundaries. Therefore, *"weak Kronecker-delta property"* is meant when the Kronecker-delta property is utilised in the remainder of the manuscript.

In conventional finite element methods the C^0-continuity which underlies the Lagrangian interpolation provides the Kronecker-delta property which is ideal for the shifting technique. With the Kronecker-delta property at hand and employing shifting, the Heaviside function will be confined to the cracked element where the nodal points are also interpolatory. The only exception is when the crack passes the location of an enriched nodal/control point, which is likely for higher-order interpolations. On the other hand, the blending technique brings the effect of the Heaviside function to the adjacent rows of elements. A drawback of this technique is indeed the presence of additional terms in nodal points, which was circumvented by the Corrected

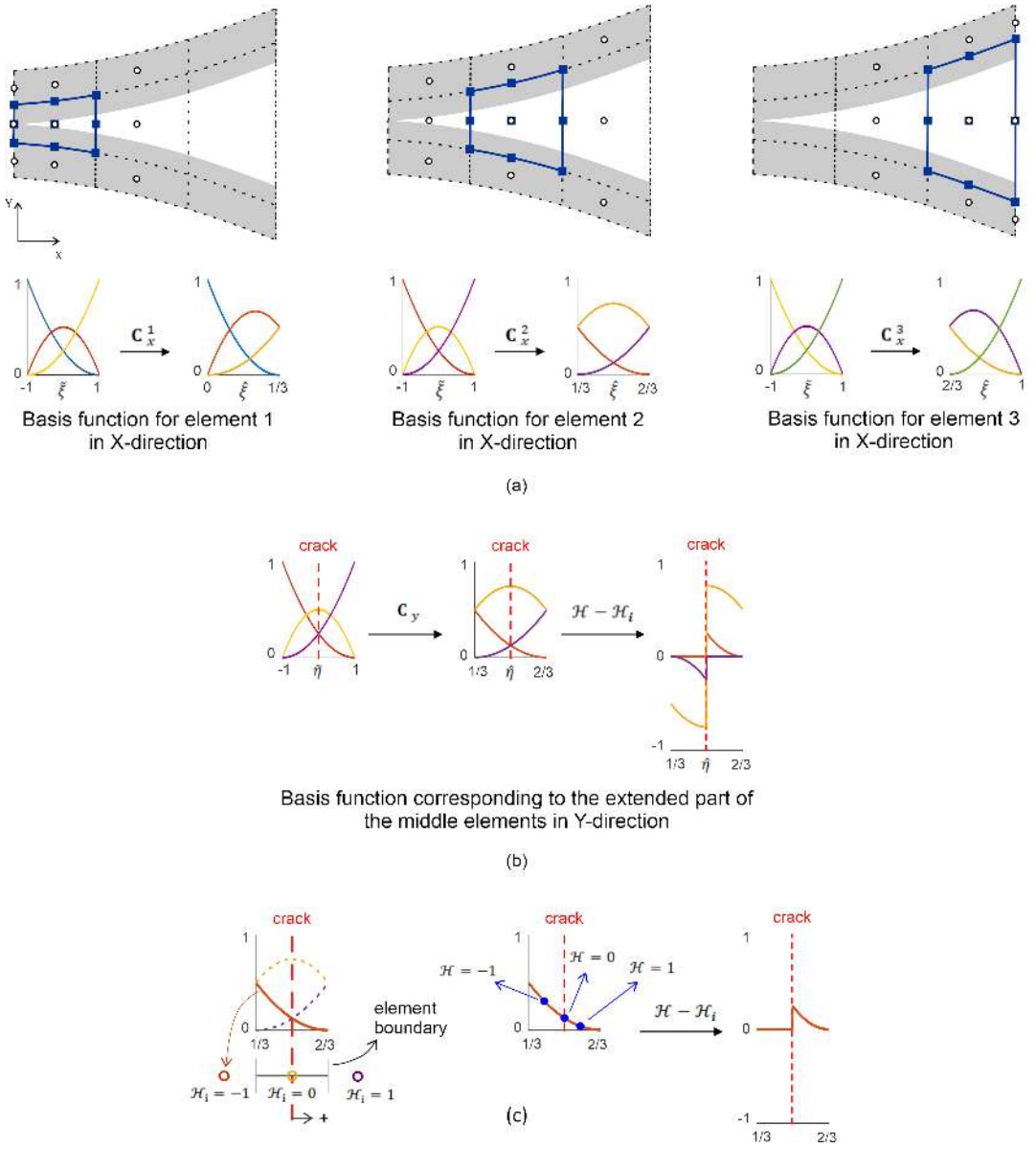

FIGURE 5 Effect of shifting on the basis functions for quadratic Bézier elements under mode-I fracture (a) in the X-direction and (b) in the Y-direction. The shifting technique is demonstrated in (c) where $\mathcal{H}$ corresponds to the Heaviside function of the Gauss point location and $\mathcal{H}_i$ indicates the Heaviside value for control points. The boundaries of each Bézier element are marked by the solid blue lines. ■ is the Bézier point, and ○ indicates the control point. Only basis functions in the *y*-direction are affected by shifting. *C* is the Bézier extraction operator.

eXtended Finite Element Method[36]. This approach effectively utilises shifting and blending concurrently perpendicular to the crack path, in order to confine the Heaviside effect and to maintain nodal points interpolatory.

Owing to the absence of the Kronecker-delta property in isogeometric analysis, shifting, which affects the extended part, will also involve adjacent rows of elements similar to blending. The number of control point rows involved perpendicular to the crack path is entirely dependent on the position of the control points and the adopted interpolation order. For example, for quadratic and cubic interpolations one row of control points at each side of the crack will be affected, while quartic and quintic interpolations will affect even two rows of control points at each side. In sum, the spread of the Heaviside effect to the adjacent elements is inevitable regardless of the technique adopted to enforce compatibility. Nevertheless, shifting and blending are still possible techniques to enforce compatibility. It is noted that the Kronecker-delta property can be brought back when considering

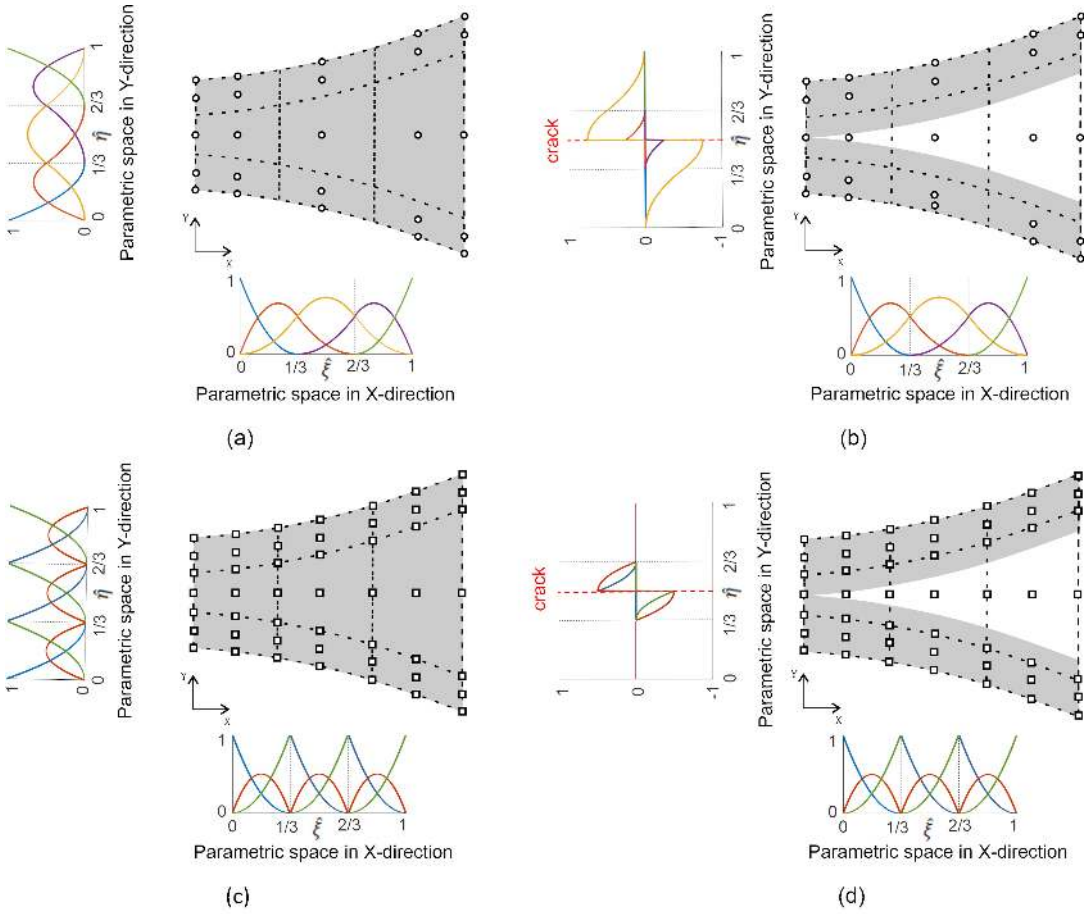

FIGURE 6 Comparison between control and Bézier points for a cracked set of quadratic elements: (a) regular basis functions for the control points, (b) extended basis functions for the control points, (c) regular basis functions for Bézier points and (d) extended basis functions for Bézier points. Here, (a) and (c) present the basis functions employed for the regular part in Equation (5), while (b) and (d) present the basis functions used for the extended part in Equation (5).

Bézier points instead of control points, which will be at the expense of lowering the continuity at element boundaries to C^0. The effect of the shifting technique for these two sets of points is compared in Figure 6. By virtue of the tensor product of the univariate bases, bivariate bases can be generated, see Figure 7 for the effect of a crack on a bivariate basis function.

The shifting technique adopted here is analogous to the blending technique employed in the extended finite element method in the direction perpendicular to the crack path, see Figures 8a, 6b and 6d, which illustrate how the presence, respectively the absence of the Kronecker-delta property affect the proposed shifting technique. Due to the fact that the crack is considered as a straight line passing through an entire element, the element size plays a significant role, since some parts of the crack may still violate the crack initiation criterion. Thus, to fulfill the initiation criterion along the crack path, yet to avoid ultra-fine meshes, a blending technique has been adopted to partially apply the cohesive rule inside a cracked element, see Figure 8. This blending technique utilises another Heaviside function in the tangential direction, a step function as a new blending, to remove integration points in front of the real crack tip, see Figures 8b and 8c. Here, the real crack tip is given in Figure 1. It is noteworthy that the enrichment is still based on the crack tip at the end of the element, compare Figure 8a where the real crack tip coincides with the end of the discontinuity and Figure 8b, where the the real crack tip is inside the element, but both have the same enrichment.

Finally, we can rewrite Equation (7) incorporating shifting and blending technique to enforce compatibility.

$$\mathbf{u}(\mathbf{x}) = \sum_{\mathcal{A}\in\mathcal{N}} \mathbf{N}_{\mathcal{A}}(\mathbf{x})\mathbf{a}_{\mathcal{A}} + \sum_{\mathcal{B}\in\mathcal{N}^{\mathcal{H}}} \mathcal{H}^{Bl}_{\Gamma_d}(\mathbf{x}) \left(\mathcal{H}^{GP}_{\Gamma_d}(\mathbf{x}) - \mathcal{H}^{\mathcal{B}}_{\Gamma_d}\right) \tilde{\mathbf{N}}_{\mathcal{B}}(\mathbf{x})\mathbf{b}_{\mathcal{B}} \tag{38}$$

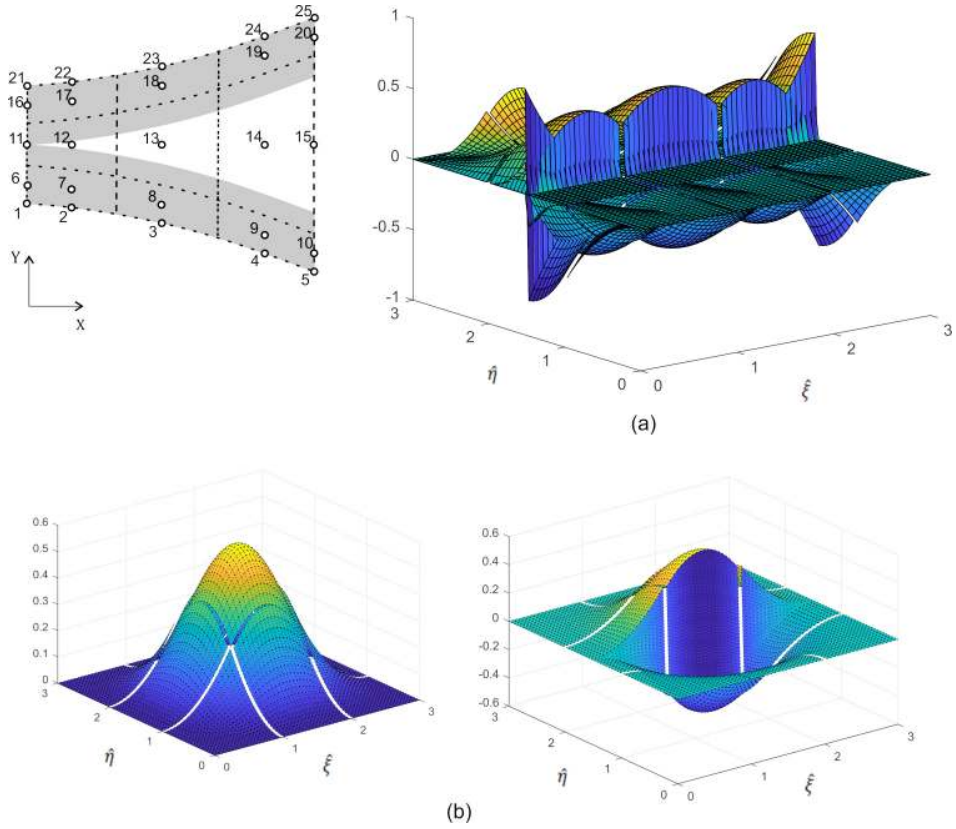

FIGURE 7 Two-dimensional basis functions for control points used in the description of a cracked medium: (a) Effect of the crack on the extended basis functions (b) Comparison between the regular (left) and the extended (right) basis functions for the point in the middle of the domain, control point 13 (see Figure 5b for a comparison with one dimensional basis functions). It is noted that the basis functions in (a) result from the tensor product of the basis functions in the X and the Y-directions in Figure 6b.

where $\mathcal{N}^{\mathcal{H}} \subset \mathcal{N}$ denoting the subset enriched by Heaviside, and $\mathcal{H}_{\Gamma_d}^{GP}$ is the Heaviside value of Gauss points, see Equation (10). $\mathcal{H}_{\Gamma_d}^{\mathcal{B}}$ indicates the Heaviside value for the control point $\mathcal{B}$, and $\mathcal{H}_{\Gamma_d}^{Bl}$ is a step function defined on the location of the Gauss point with respect to *real crack tip* rather than *crack tip* in Figures 8b and 8c:

$$\mathcal{H}_{\Gamma_d}^{Bl} = \begin{cases} 0 \text{ if } \dfrac{\mathbf{v}\cdot\mathbf{n}_{rct}}{\|\mathbf{v}\|\|\mathbf{n}_{rct}\|} \geq 0 \\ \\ 1 \text{ if } \dfrac{\mathbf{v}\cdot\mathbf{n}_{rct}}{\|\mathbf{v}\|\|\mathbf{n}_{rct}\|} < 0 \end{cases} \tag{39}$$

4.3 | Discretised and linearised equations

Substituting Equations (7) and (11) for the displacement and the strain fields expressed in discrete values, into the weak forms of Equations (24a) and (24b), the discrete form of the equation of motion can be derived:

$$\int_{\Omega} \mathbf{B}^{\mathbf{T}}\boldsymbol{\sigma}\mathrm{d}\Omega = \int_{\Gamma_u} \mathbf{R}^{\mathbf{T}}\bar{\mathbf{t}}\mathrm{d}\Gamma \tag{40a}$$

$$\int_{\Omega} \mathcal{H}_{\Gamma_d}\tilde{\mathbf{B}}^{\mathbf{T}}\boldsymbol{\sigma}\mathrm{d}\Omega + 2\int_{\Gamma_d} \tilde{\mathbf{R}}^{\mathbf{T}}\mathbf{t}_d\mathrm{d}\Gamma = \int_{\Gamma_u} \mathcal{H}_{\Gamma_d}\tilde{\mathbf{R}}^{\mathbf{T}}\bar{\mathbf{t}}\mathrm{d}\Gamma. \tag{40b}$$

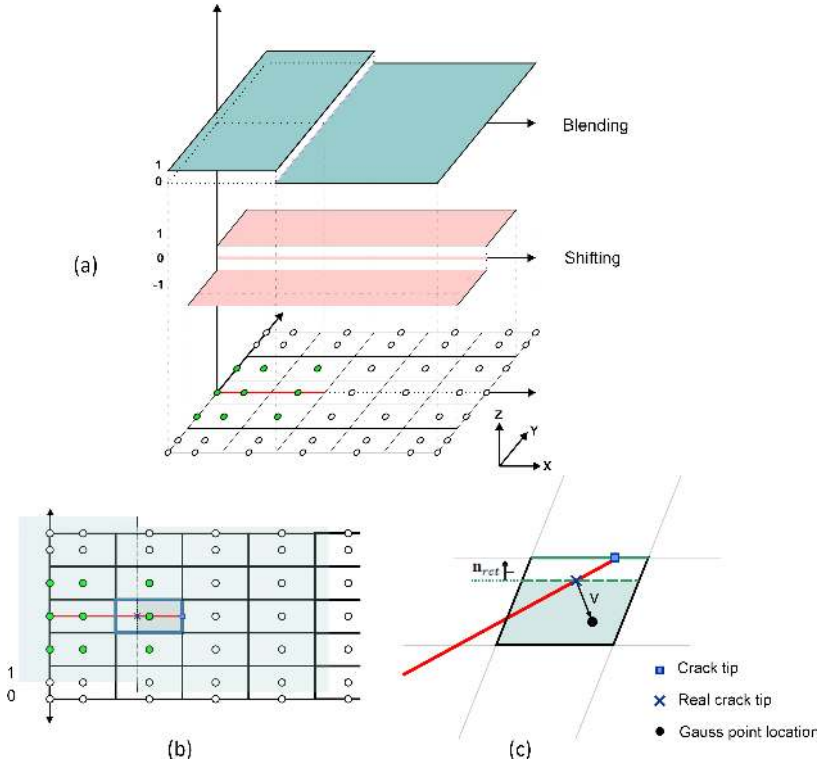

FIGURE 8 Compatibility enforcement for a quadratic interpolation under mode-I fracture: (a) shifting and blending technique for a fully cracked element, (b) blending technique for a partially cracked element while the crack is aligned with the mesh and (c) blending technique for a partially cracked element with an inclined discontinuity. The integration border, dashed green line in (c), is defined as the edge shifted from the green solid line.

Considering Equation (14), the stress in the bulk away from the discontinuity reads:

$$\boldsymbol{\sigma} = \mathbf{D}\boldsymbol{\epsilon} = \mathbf{D}\left(\mathbf{B}\mathbf{a} + \mathcal{H}_{\Gamma_d}\tilde{\mathbf{B}}\mathbf{b}\right) \tag{41}$$

and the traction at the discontinuity is defined in Equation (17) where the displacement jump based on the adopted Heaviside function in Equation (10) is:

$$[\![u_d]\!] = 2\sum_{k=1}^{n_{en}} \tilde{R}_k(\xi) b_k \tag{42}$$

with n_{en} the number of enriched nodes. $\tilde{R}_k$ is the NURBS set of basis functions corresponding to the extended part. Employing linearisation and discretisation then results in the following matrix-vector equation:

$$\begin{bmatrix} \mathbf{K}_{aa} & \mathbf{K}_{ab} \\ \mathbf{K}_{ab} & \mathbf{K}_{bb} \end{bmatrix} \begin{bmatrix} \Delta\mathbf{a} \\ \Delta\mathbf{b} \end{bmatrix} = \begin{bmatrix} \mathbf{f}_a^{\text{ext}} \\ \mathbf{f}_b^{\text{ext}} \end{bmatrix} - \begin{bmatrix} \mathbf{f}_a^{\text{int}} \\ \mathbf{f}_b^{\text{int}} \end{bmatrix} \tag{43}$$

with the arrays

$$\mathbf{f}_a^{\text{ext}} = \int_{\Gamma_u} \mathbf{R}^{\mathrm{T}}\bar{\mathbf{t}}\,\mathrm{d}\Gamma \tag{44a}$$

$$\mathbf{f}_b^{\text{ext}} = \int_{\Gamma_u} \mathcal{H}_{\Gamma_d}\tilde{\mathbf{R}}^{\mathrm{T}}\bar{\mathbf{t}}\,\mathrm{d}\Gamma \tag{44b}$$

$$\mathbf{f}_a^{\text{int}} = \int_{\Omega} \mathbf{B}^{\mathrm{T}}\boldsymbol{\sigma}\,\mathrm{d}\Omega \tag{44c}$$

$$\mathbf{f}_b^{\text{int}} = \int_{\Omega} \mathcal{H}_{\Gamma_d}\tilde{\mathbf{B}}^{\mathrm{T}}\boldsymbol{\sigma}\,\mathrm{d}\Omega + 2\int_{\Gamma_d} \tilde{\mathbf{R}}^{\mathrm{T}}\mathbf{t}_d\,\mathrm{d}\Gamma \tag{44d}$$

and stiffness matrices:

$$\mathbf{K}_{\mathrm{aa}} = \int_{\Omega} \mathbf{B}^{\mathbf{T}}\mathbf{D}\mathbf{B}\mathrm{d}\Omega \tag{45a}$$

$$\mathbf{K}_{\mathrm{ab}} = \int_{\Omega} \mathcal{H}_{\Gamma_d}\mathbf{B}^{\mathbf{T}}\mathbf{D}\tilde{\mathbf{B}}\mathrm{d}\Omega \tag{45b}$$

$$\mathbf{K}_{\mathrm{ba}} = \int_{\Omega} \mathcal{H}_{\Gamma_d}\tilde{\mathbf{B}}^{\mathbf{T}}\mathbf{D}\mathbf{B}\mathrm{d}\Omega \tag{45c}$$

$$\mathbf{K}_{\mathrm{bb}} = \int_{\Omega} \tilde{\mathbf{B}}^{\mathrm{T}}\mathbf{D}\tilde{\mathbf{B}}\,\mathrm{d}\Omega + 4\int_{\Gamma_d} \tilde{\mathbf{R}}^{\mathrm{T}}\mathbf{Q}^{\mathrm{T}}\mathbf{T}_d\mathbf{Q}\tilde{\mathbf{R}}\,\mathrm{d}\Gamma \tag{45d}$$

while it is recalled that $\mathbf{Q}$ is the rotation matrix. It is important to note that shifting and blending are employed in the numerical integration level of the current equations, according to Equation (38).

5 | IMPLEMENTATION ASPECTS

The implementation of the formulation in a finite element data structure requires care, since isogeometric analysis involves inter-element sharing of control points. Moreover, the possibility to adjust the order of continuity, and consequently the number of control points shared by two adjacent elements complicates a unique solution to the problem. Therefore, we have examined various options to check these issues. We note that elements are here defined as sections generated by intersecting C^0 lines in the physical space.

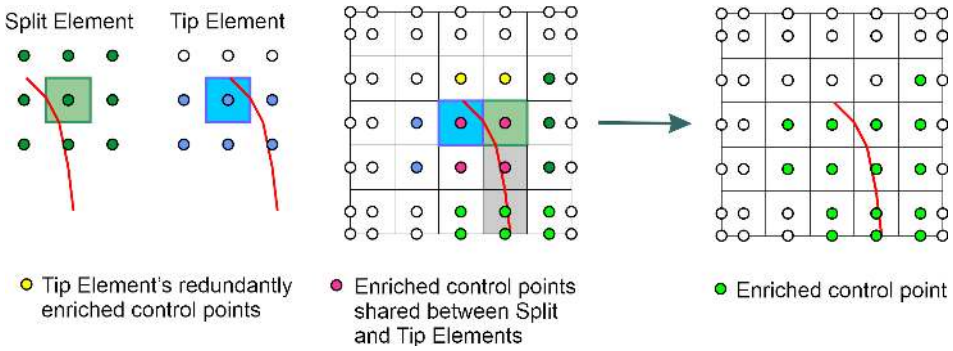

FIGURE 9 Enrichment scheme for a quadratic discretisation. The yellow control points which are shared between split elements (green) and tip element (blue) have been removed from the enrichment.

5.1 | Enhancement of individual control points and the integration scheme

While the inter-element sharing of control points complicates element-wise enrichment in isogeometric analysis, the Kronecker-delta property of the Bernstein basis functions mitigates the problems encountered in enrichment procedure. Since we deal with cohesive-zone models there is no singularity at the crack tip, and hence no need to apply asymptotic tip enrichment functions. As is also customary in extended finite element analysis using cohesive-zone models, the crack is assumed to cross the element entirely and the crack tip is not considered as opened. The edge where the crack tip lies is denoted as *tip edge*. For C^0 elements with the Kronecker-delta property, the control points corresponding to the tip edge are not enriched. However, for elements with higher-order continuity, the enrichment relies on the continuity order at element boundaries. The control points located at, or in front of the tip edge should be neglected for the enrichment, see Figure 9. Our experiments reveal divergence of the solution if only the last column of control points is omitted in the enrichment, which is described in the ensuing sections.

To approximate the discontinuous field in a cracked element, an adequate integration scheme at each side of the discontinuity should be applied. A frequently used scheme is sub-triangulation. This approach is believed to be superior to other methods,

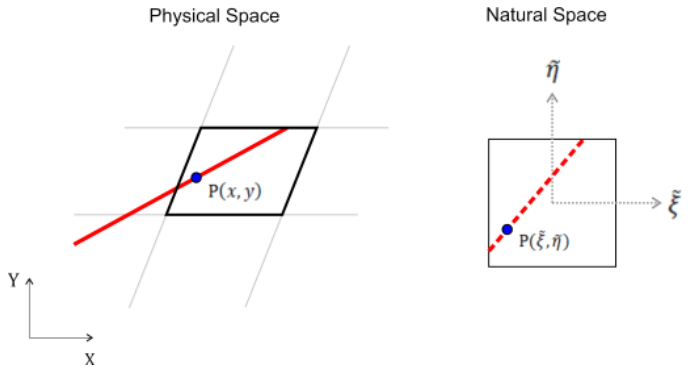

FIGURE 10 Finding the unknown natural coordinates, $\mathrm{P}(\tilde{\xi}, \tilde{\eta})$, of a known physical point, $\mathrm{P}(x, y)$, along the crack.

e.g. the cell approach, since it is separately defined for each section generated by the crack. Therefore, adopting a required minimum number of Gauss points for each sub-triangle guarantees a sufficient number of Gauss points at each side, even if the discontinuity splits the element into disproportionate segments, e.g. if the crack path is close to the corner of an element. Geometrical mapping for these triangles within an isogeometric analysis framework has been presented by Ghorashi *et al.* [25].

5.2 | Point projection along the crack path

In cohesive fracture, a line integration is required to integrate the traction which acts at the discontinuity. Gauss integration is also used for this purpose. As observed in Figure 4, Bézier extraction maps a point in the physical space onto the parameter domain in the Bernstein parent element. Nevertheless, finding the corresponding natural coordinates of a physical known point necessitates a point projection [37], see Figure 10. Herein, a Newton-Raphson scheme has been utilised to obtain solution, see Appendix B for the case of NURBS.

6 | ASSESSMENT OF THE FORMULATION

We now assess the correctness and the properties of the formulation and implementation aspects at the hand of various examples.

6.1 | Interpolation-order: uniform opening

The first example challenges the capability of the extended isogeometric formulation to handle different interpolation orders for the standard and the extended contributions. This is done using a simple tension test and is compared to a solution obtained using standard interface elements. The geometry and material properties are shown in Figure 11. A dummy stiffness has been adopted to constrain the interface before opening.

For higher-order extended finite element methods the same order of interpolation can be adopted for the regular and the enhanced parts [15,22]. For different orders the method only works when a linear interpolation is applied to the extended part [15,21]. Otherwise, when using blending for the direction perpendicular to the discontinuity, the error in the blending elements will increase and affect the solution accordingly [15]. The Corrected eXtended Finite Element Method [36] is a remedy [15], and involves a shifting for the interpolations which possess the Kronecker-delta property.

For eXtended IsoGeometric Analysis, De Luycker *et al.* [24] have arrived at the same conclusions for the case of the same orders of interpolation, and have chosen a linear interpolation for the extended part in the case of different orders of interpolation. Nevertheless, they have reported convergence issues even with linear interpolation for the extended part, and have suggested C^0 lines as a possible remedy.

We first investigate the case of the same interpolation order for the standard and the extended parts. This is examined for higher-order continuity as well as C^0 continuity at the boundaries of the element. The load-displacement curve in Figure 12 agrees with the conclusions reported before [22,15,24].

Next, we examine the case where different interpolation orders are taken for the standard and extended parts. Again, the cases of higher-order continuity and C^0 continuous elements are investigated. Figure 13 shows that, when higher-order continuity

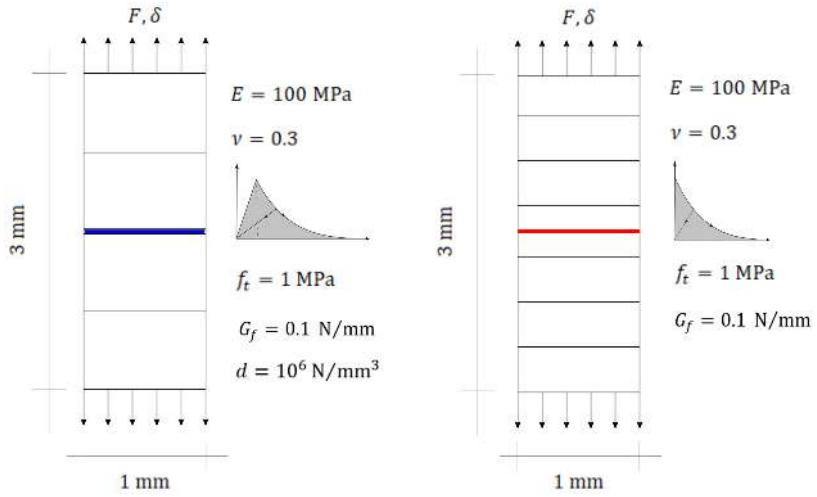

FIGURE 11 Geometry and traction-separation relation employed in the interface element model (left figure) and the XIGA model (right figure). The dummy stiffness d is utilised to keep the interface element closed until the criterion for fracturing is met. F and δ denote the force and the displacement, respectively.

is used for both parts, the error is considerable. When using C^0 continuity, however, the errors are small and the solution is acceptable. Yet, only a linear interpolation for the extended part reproduces the finite element results. Accordingly, the use of linear interpolation for the extended part, which produces perfect results for extended finite element methods [15,21] is fully correct in extended isogeometric analysis only when C^0-continuity is adopted [24]. This is reminiscent of results for isogeometric interface elements, where traction oscillations could also be prevented by inserting C^0 lines [11], as a possible remedy.

6.2 | Effect of the order of continuity on the enrichment: peeling test

A Double Cantilever Beam (DCB) peeling test is now investigated to assess the effect of the interpolation order on the enrichment scheme. The geometry is shown in Figure 14. The Young's modulus, Poisson's ratio, tensile strength and fracture energy are $E = 100$ MPa, $\nu = 0.3$, $f_t = 1$ MPa and $G_f = 0.1$ Nmm^{-1}, respectively. For the interface elements, which serve as the benchmark, the dummy stiffness, $d = 10^6$ Nmm^{-3}, is used to keep the interface closed until the crack propagation criterion is satisfied.

A comparison between the enrichment schemes for different orders of continuity is given in Figure 15. For presentation purposes, the enrichment is illustrated for a 7× 7 mesh, instead of the DCB. Following Section 5.1, control points with a location at or in front of the tip edge are removed from the enrichment. When utilising C^0 continuity, however, only one column of control points at the tip edge will be eliminated from enrichment regardless to interpolation order, see Figure 15, where the control points and Bézier points are represented by circles and squares, respectively. We observe that, when using control points, only one row at the tip edge is not enriched for linear interpolation. This is the same for quadratic interpolation: remove one column of control points in front of the crack tip. For cubic interpolation, however, two columns of control points are not enriched. Control/Bézier points belonging to the tip element are marked in blue, while the enriched points are filled with green, see Figure 15.

The results are given in Figure 16. For a quadratic interpolation (Figure 15.c), C^1-continuity at the element boundaries provides smoother results compared to C^0-continuity (Figure 15.d). It can be inferred that, when enriching the same number of control/Bézier points, smoother results are obtained in the case of control points. For a cubic interpolation, however, a jagged response results for the 60×9 (the first and the second digits denote the number of element in length and width of the Double Cantilever Beam, respectively) and 120×9 meshes alike. This is because one extra column of control points is removed for the enrichment in the case of a C^2-continuity compared to a C^0-continuity, see Figure 15.

To clarify the reason behind the jagged response reported in Figure 16c, higher order interpolations are compared separately in Figure 17. For cubic-cubic and quartic-quartic results it is observed that when the crack propagates to the next element, the last split element releases suddenly along with the last crack tip (which is the new split element adjacent to the new tip element). The release of two elements instead of one (the last crack tip) causes the jagged response. Therefore, a drop is observed whenever

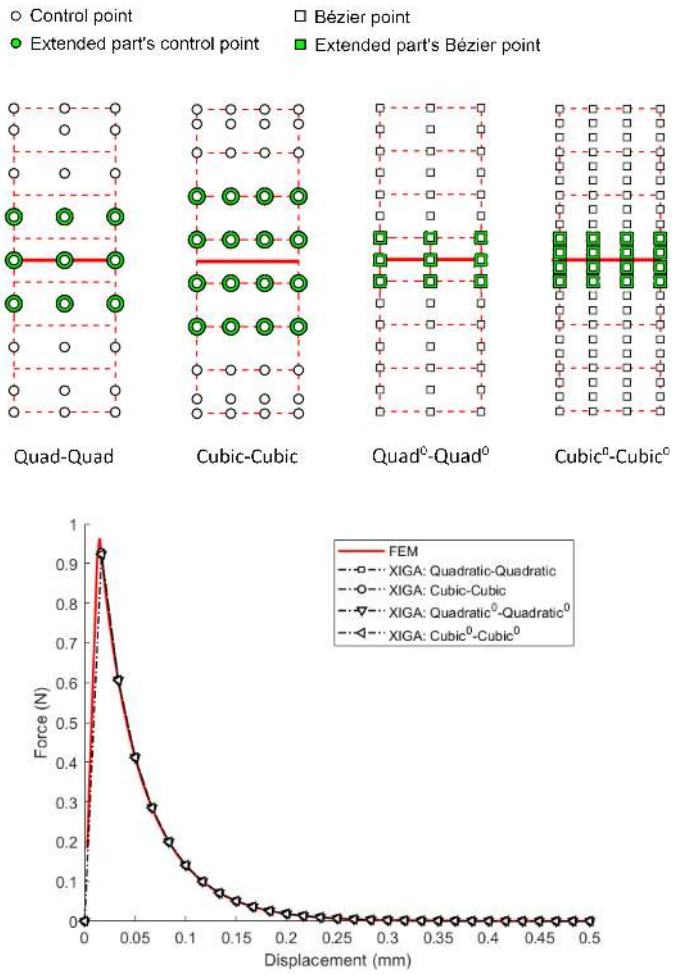

FIGURE 12 Discretisation and load-displacement curve for the uniform opening problem with the same order for standard and extended parts. The first and second interpolation terms (left to right) in the figure belong to the standard and extended parts, respectively. A superscript zero denotes the Bézier elements. Circles indicate the control points and squares denote the Bézier points. Enriched points are specified with the filled green marker. It is noted that the enriched control points coincide with those belonging to the cracked element. It is noted that FEM solution denotes the interface element model in the remainder of the manuscript, see Figure 11.left.

the crack propagates to a new element. This is not the case for quadratic-quadratic since all the control points associated with the split element adjacent to the tip element are enriched. Hence, this phenomenon is related to the number of control point columns. If there is more than one column of control points removed from the enrichment we will have a split element that is not fully enriched. For the same number of control point columns removed, the quartic interpolation has a smoother behaviour than the cubic interpolation, as observed in Figure 17.

Regarding Figures 16b and 16d, some slight oscillations are observed. This is because we consider the propagation criterion for only the half the number of Gauss points along the crack path, since otherwise the element would have remained intact. This is also the reason why two tips are defined: one ending at the element edge *crack tip*, and another located at the nearest Gauss point to the tip which has met the fracture criterion $\sigma \geq f_t$ as *real crack tip*, see Figure 1b. Note that the *crack tip* is utilised for the enrichment of control points, while the *real crack tip* is defined for the blending technique in order to avoid considering the section of the crack where the fracture criterion has not yet been satisfied (blue Gauss points in Figure 1b with $\sigma < f_t$). As mentioned in the preceding, an ultra-fine mesh is required, where all Gauss points along the hypothetical crack path have met the propagation criterion, in order to obtain a smooth force-displacement response. The results of such an approach are shown in Figure 18. For the quadratic-quadratic case, the difference between the blue and the yellow marks shows the sensitivity of the

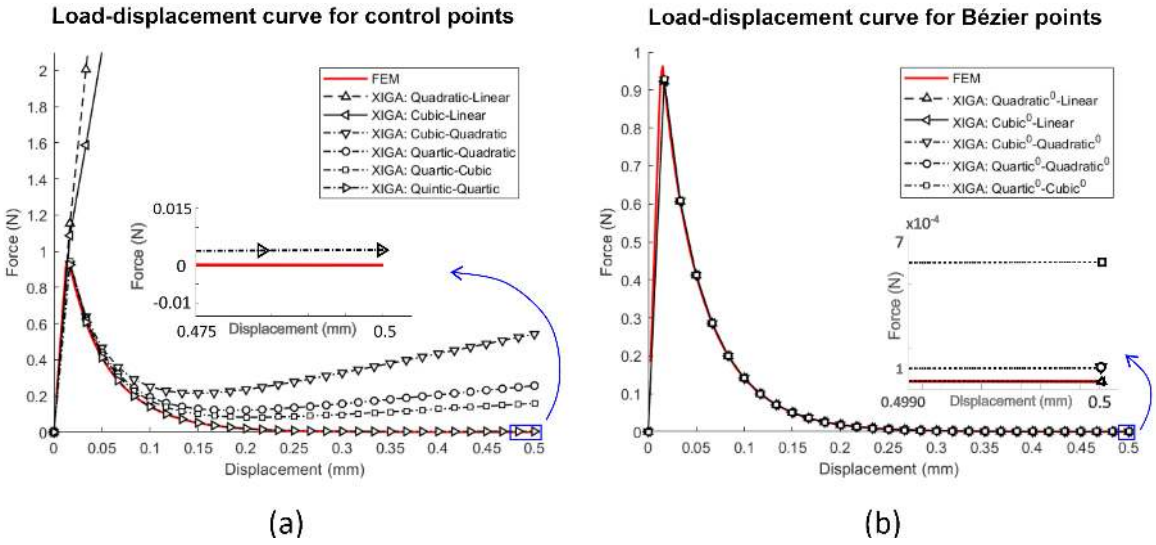

FIGURE 13 Discretisation and load-displacement curve when different interpolation orders are adopted for the standard and extended parts. Higher-order continuity (left) and the Kronecker-delta property (right) are compared through different orders adopted for the standard and extended part. A superscript zero denotes the Bézier elements.

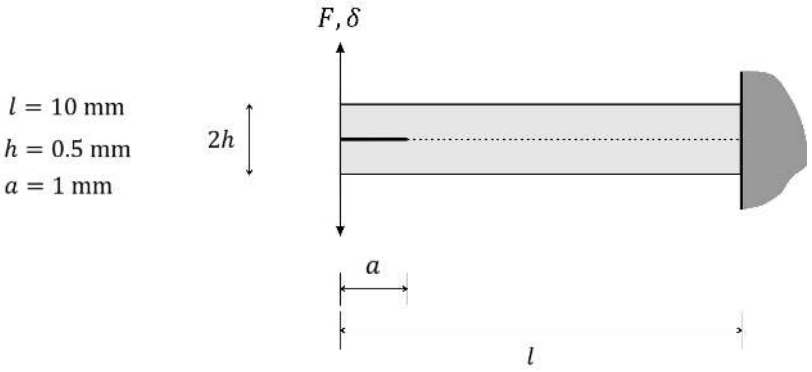

FIGURE 14 Double Cantilever Beam with an initial notch subjected to mode-I loading.

solution to the size of the mesh. Since the quadratic − quadratic and quadratic^0 − quadratic^0 show the least jagged responses, we have used them in ensuing sections.

6.3 | Infinite plate with a circular void

While several meshing techniques are available in finite element analysis, the discretisation in isogeometric analysis is less straightforward, and may involve multi-patches even for fairly simple geometries. Since multi-patches typically require additional care to deal with stress continuity between shared surfaces/edges, it can affect the robustness of the solution. Accordingly, techniques such as the Finite Cell Method[13] or Level Sets may be competitive for modelling, e.g., voids.

Herein, we apply the Level Set technique to a void. The geometry is given in Figure 19. Quadratic interpolation has been adopted for both standard and extended parts. For the void level set, the degrees of freedom which correspond to control points which have no influence on the elements of the solid, should be removed from the system of equations, and those belonging to the elements outside the void should be treated as normal degrees of freedom, see Figure 20a. The remaining elements are those crossed by the discontinuity (void's edge), therefore they are partially inside the void. Control points corresponding to this type of elements will be enriched and a weighting function should be defined to partially inactivate the section inside the void. To

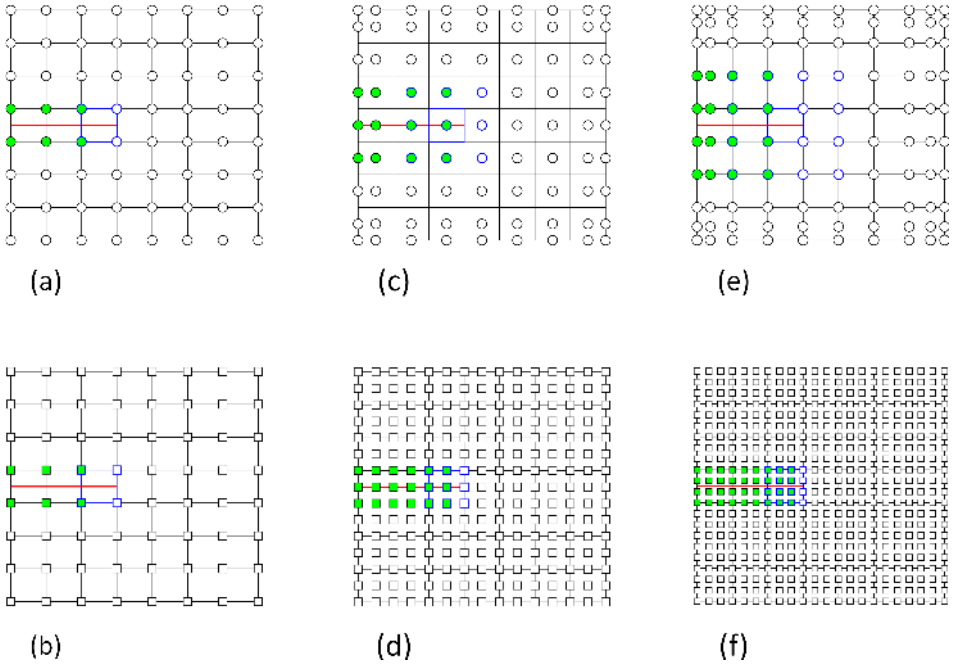

FIGURE 15 Comparison of the enrichment for different interpolation orders: (a) linear control points, (b) linear Bézier points, (c) quadratic control points, (d) quadratic^0 Bézier points, (e) cubic control points, (f) cubic^0 Bézier points. Control/Bézier points belonging to the tip element are marked in blue, while the enriched points are filled with green. Note that (a) and (b) are the same and are only presented separately for the sake of compatibility with other cases.

this end, a step function similar to the blending Heaviside function, Equation (38), is defined, where control points inside the void take the value 0, while those outside take the value 1.

If the discontinuity crosses an element such that it is divided disproportionally (e.g. close to a corner), the stiffness matrix can become singular. Defining positive and negative parts as in Figure 3 for the elements crossed by the discontinuity, enrichment should only be done if:

$$\frac{A^{\Omega^-}}{A^{\Omega^-\cup\Omega^+}} \quad \text{and} \quad \frac{A^{\Omega^+}}{A^{\Omega^-\cup\Omega^+}} > \epsilon \tag{46}$$

where $\epsilon = 10^{-3}$ has been used, since smaller values resulted in singularity of the tangent stiffness matrix. Accordingly, some elements were exempted from the enrichment, namely the dashed magenta elements in Figure 20b, while the elements with blue edges are enriched. Priority in enrichment for the shared control points is given to the blue-edged elements. To further clarify, the enrichment of two adjacent elements with shared control points are illustrated in Figure 20b. We observe that the yellow element should not be enriched, but the shared control points between this element and the green element are enriched because of the priority given to the blue-edged element. This will result in the only magenta control point not being enriched for the yellow element, see the specified yellow element at the right hand side of the zoom Figure 20b.

The results of the void level set approach are compared with those where the void has been modelled explicitly, also using NURBS shape functions and show a good agreement between both approaches in terms of displacements and stresses, Figure 21.

7 | MORE COMPLICATED 2D FRACTURE PROBLEMS

Below we will consider two further cases, to demonstrate the capability of the formulation to handle crack and void concurrently, and to assess the ability to analyse the propagation of curved cracks. The traction-separation relation of (1) has been employed.

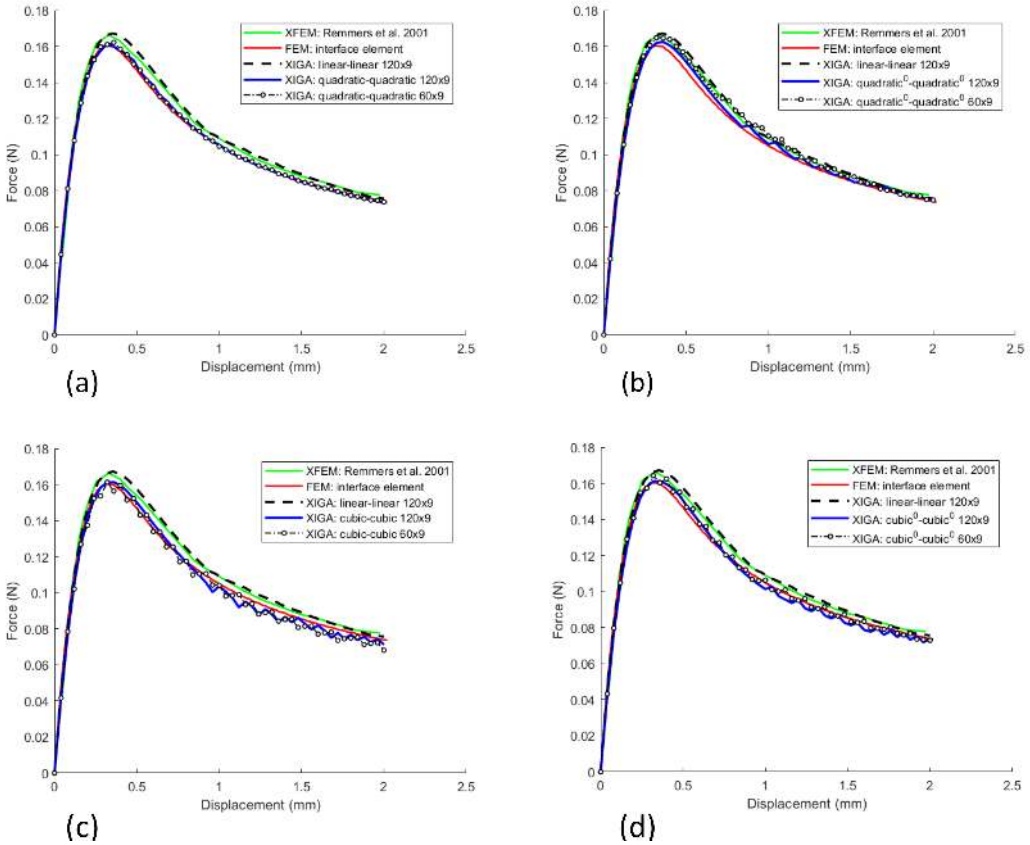

FIGURE 16 Results of the peeling test for a DCB with the same order adopted for both standard and extended part. (a) Results for quadratic interpolation, (b) results for quadratic^0 interpolation, (c) results for cubic interpolation, (d) results for cubic^0 interpolation.

7.1 | Straight crack propagation: wedge splitting test

A wedge with an initial void and a notch is considered. Although the crack path is known, we allow the crack to propagate freely. The geometry is illustrated in Figure 22 with a thickness of 400 mm. A void level set has been used to generate the notch. Also, a C^0 line has been added at the location of the force to enforce the Neumann boundary condition. The material properties are as follows: Young's modulus $E = 28,300$ MPa, Poisson's ratio $\nu = 0.18$, tensile $f_t = 2.11$ MPa and fracture energy $G_f = 0.482$ Nmm^{-1}. A quadratic-quadratic has been adopted.

Figure 22 compares the current results with those obtained using an XFEM-like approach[38], although a dummy stiffness was used to keep the crack closed before crack opening, similar to interface elements. Using the same material properties, the present results appear to be closer to the experiment.

7.2 | Arbitrary crack propagation: L-shaped beam

Finally, free crack propagation is examined for an L-shaped beam, shown in Figure 23, with a thickness equal to 100 mm. Material properties are given as: Young's modulus $E = 20$ GPa, Poisson's ratio $\nu = 0.18$, tensile strength $f_t = 2.5$ MPa and fracture energy $G_f = 0.13$ Nmm^{-1}. A void level set has been used to generate the geometry, see Figure 23. A C^0 line (in magenta) has been added at the location of the force to easily enforce the Neumann boundary condition. The other C^0 lines (in black) have been added to align the mesh with the void in order to avoid crack-void interaction.

Based on the results of Figure 16 a quadratic^0 − quadratic^0 interpolation has been chosen. The difficulty of the example lies in the role of the stress distribution, where small variations can lead to significant changes in the direction of crack propagation. Although isogeometric analysis exploiting B-splines vastly improves the stress prediction, using a non-local averaging method as

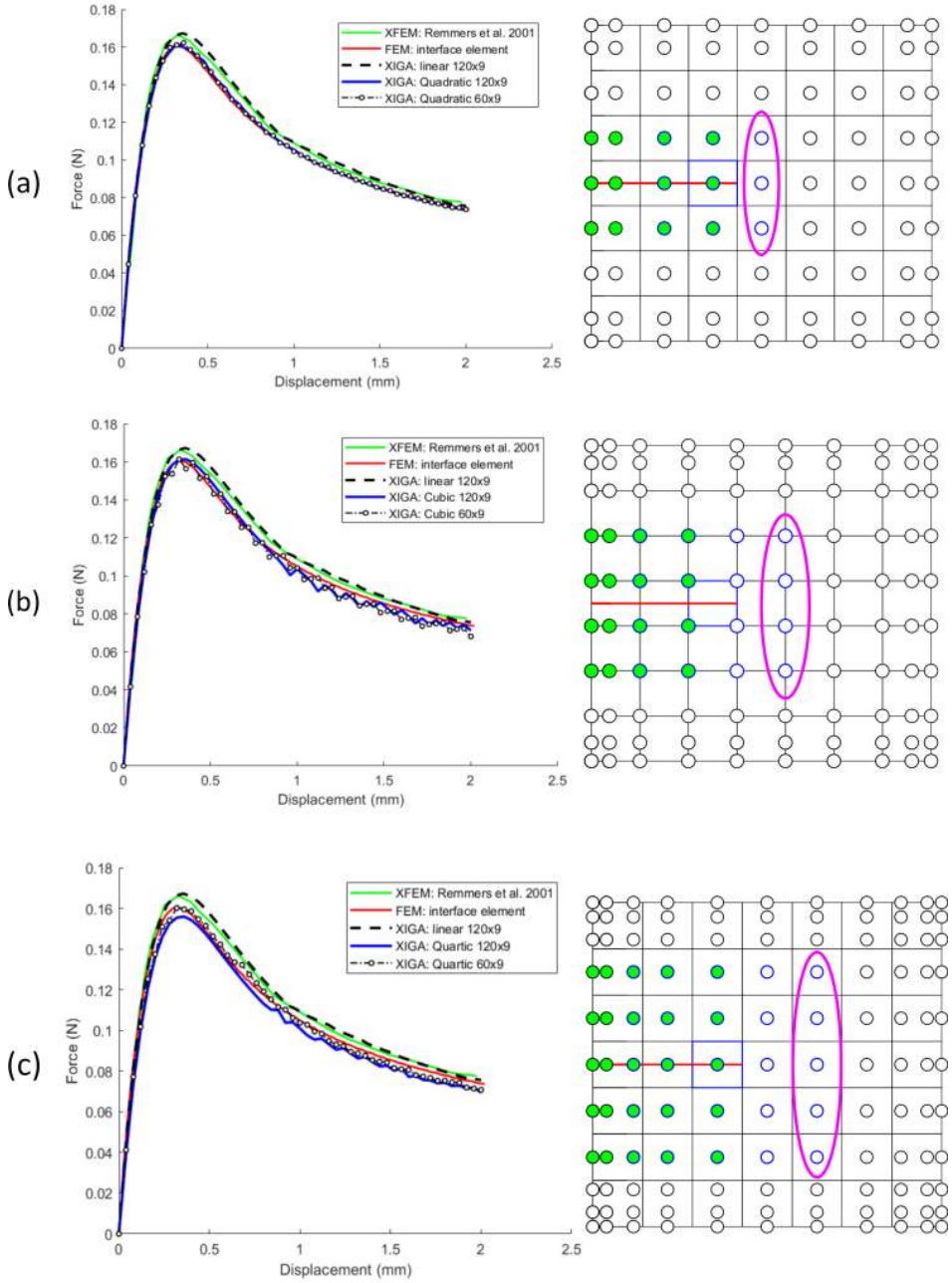

FIGURE 17 Comparison between (a) quadratic-quadratic, (b) cubic-cubic and (c) quartic-quartic interpolations for a Double Cantilever Beam. The last column of control points are illustrated with the magenta marker.

detailed before can often be beneficial to improve the crack path. Indeed, the crack extension is highly sensitive to the computed stress distribution around the crack tip[39,38]. In turn, the stress distribution depends on numerical issues like the length scale over which averaging is done, the number of Gauss points and the adopted continuity order. Therefore, even non-local averaging of stresses may not lead to sufficiently accurate measures to properly predict the crack path[38]. This can result in drastic changes in the crack path which have been already reported for XFEM[39,38], and can include a doubling back of the crack on its original path.

The results are shown in Figure 24. A behaviour similar to extended finite elements[39] and Powell-Sabin B-splines[14] is observed. An abrupt change occurs in the propagation direction, as shown in Figure 24a, which is not the case for T-splines[13]. Apart from the sensitivity of the non-local approach to find the proper crack extension direction, the order of continuity adopted

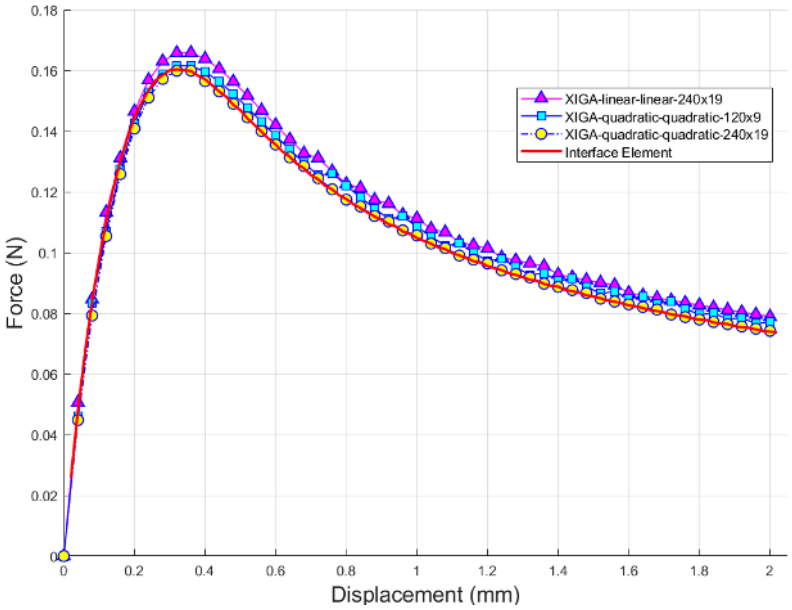

FIGURE 18 Double Cantilever Beam with an ultra-fine mesh and all GPs for crack propagation inside an element.

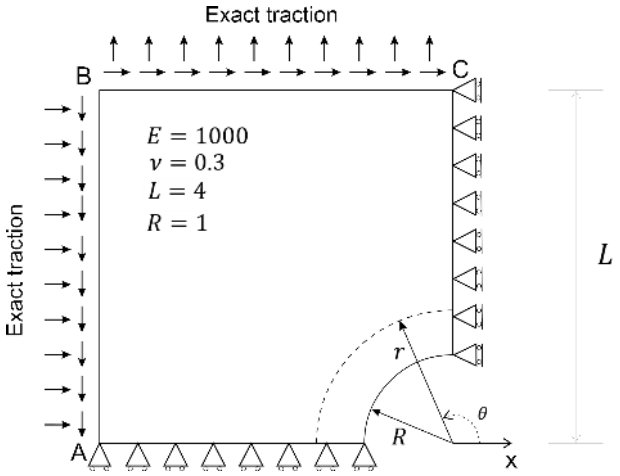

FIGURE 19 Infinite plate with a circular hole subjected to tractions at the boundaries, $\bar{\mathbf{t}}_{\mathrm{AB}} = \left(-\sigma_{xx}, -\sigma_{xy}\right)$ and $\bar{\mathbf{t}}_{\mathrm{BC}} = \left(\sigma_{xy}, \sigma_{yy}\right)$.

for the crack path therefore also appears to play a role. T-splines exploit their higher-order continuity property [13], resulting in a smooth crack path, as illustrated in Figure 25.

To validate the extended isogeometric analysis approach for curved crack propagation, and to examine the behaviour of the smooth crack path, we have therefore enforced the crack path to become straight before an erratic change in the path, i.e. the red dashed line deviating from the solid red line in Figure 24a and the cyan solid line in Figure 24c. Then, results are obtained which are close to those obtained using Powell-Sabin B-splines, see the red dashed line in Figure 24b, while the red solid line has been terminated around 5 KN.

8 | CONCLUDING REMARKS

An extended isogeometric analysis (XIGA) procedure has been developed for cohesive fracture by adding an additional blending technique which is also capable of locating a more realistic crack tip position inside an element. Moreover, in the direction

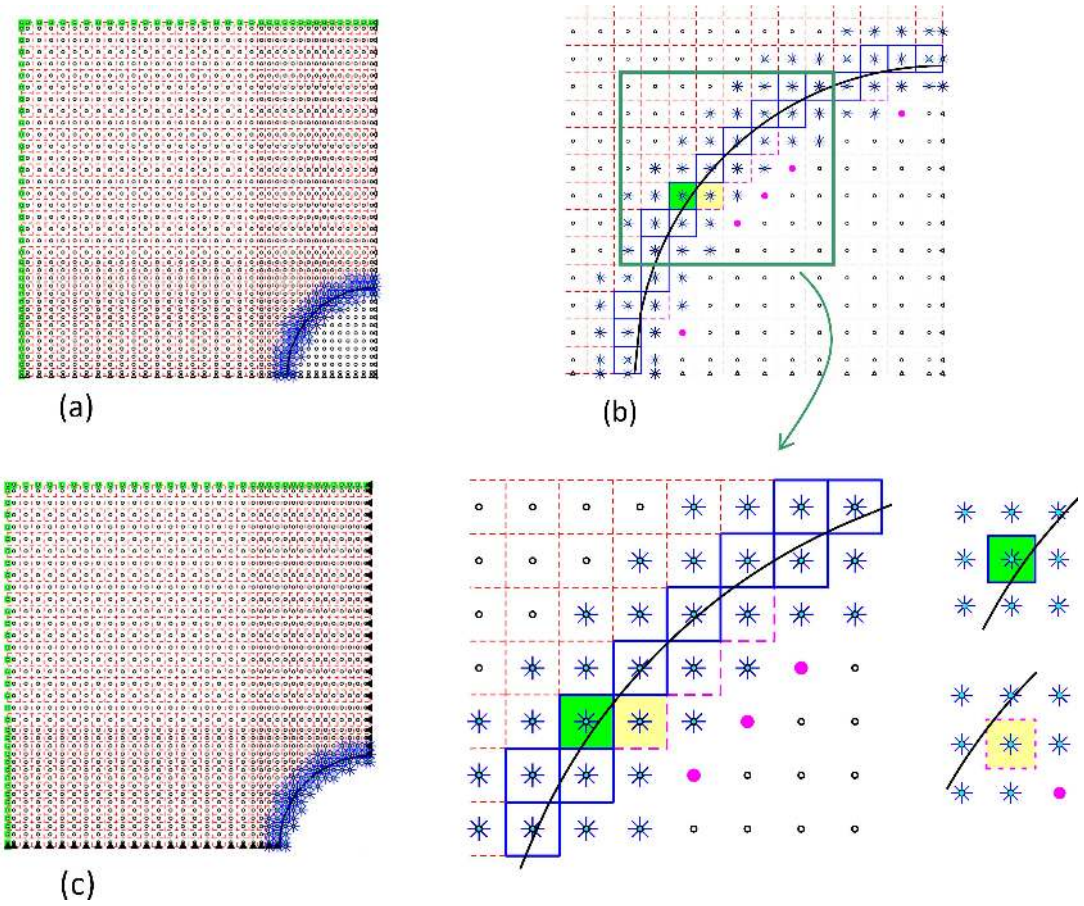

FIGURE 20 Void level set for a perforated plate. (a) Control points of the elements passed by the discontinuity are enriched and those inside the void are not; (b) Removed elements and enrichment owing to a disproportionate split: dashed magenta edges and their corresponding control points (filled with magenta) belong to eliminated elements, while the solid blue edges indicate the enriched elements; (c) Degrees of freedom belonging to control points inside the hole are eliminated from the system of equations. C^1 quadratic interpolation has been adopted for the standard and the extended parts.

perpendicular to the crack path, shifting has been utilised to ensure compatibility with the remainder of the mesh. To ensure compatibility with standard finite element data structures Bézier extract has been used and in this way the method comes close to an extended finite element method. Compared to the latter, complications ensue, however, since the higher-order continuity of B-splines and NURBS used in extended isogeometric analysis affect more rows of elements parallel to the crack when using a shifting technique to ensure compatibility of the cracked elements with the neighbouring elements, and since the Kronecker-delta property does not hold anymore. The latter observation is the reason why blending has been introduced ahead of the crack tip.

The accuracy with respect to different orders of continuity for the regular and extended parts of the displacement field has been investigated at the hand of a simple tension test. It has been shown that, when using the same order for both parts, the extended isogeometric analysis approach works perfectly irrespective of the order of continuity at the boundaries of the elements. For a different order of continuity, however, Bézier points (C^0-continuity at element boundaries) should be used for both parts. The differences encountered when either enriching control or Bézier points have been assessed for a peel test. The method has also been shown to give excellent results for a plate with a hole, for crack-void interaction and for arbitrary crack propagation in an L-shaped beam.

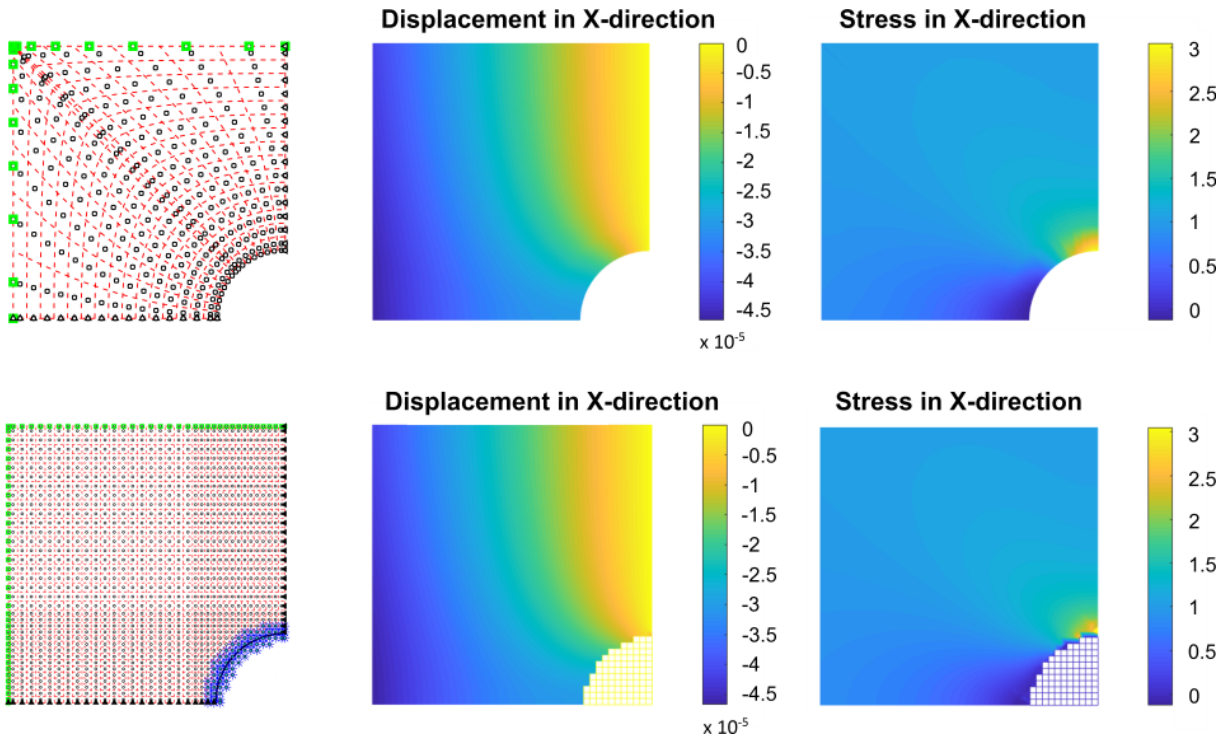

FIGURE 21 Comparison between explicit modelling of the void (first row) and modelling the void using extended isogeometric analysis (second row).

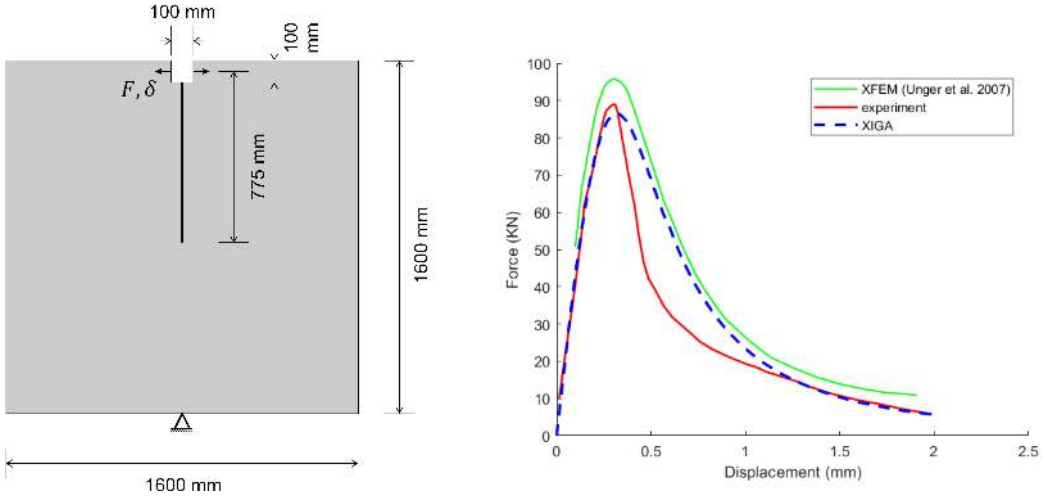

FIGURE 22 Wedge splitting test: geometry and results.

ACKNOWLEDGMENTS

Financial support from the European Research Council (Advanced Grant 664734 "PoroFrac") is gratefully acknowledged.

CONFLICT OF INTEREST

The authors declare that there is no conflict of interest regarding the publication of this paper.

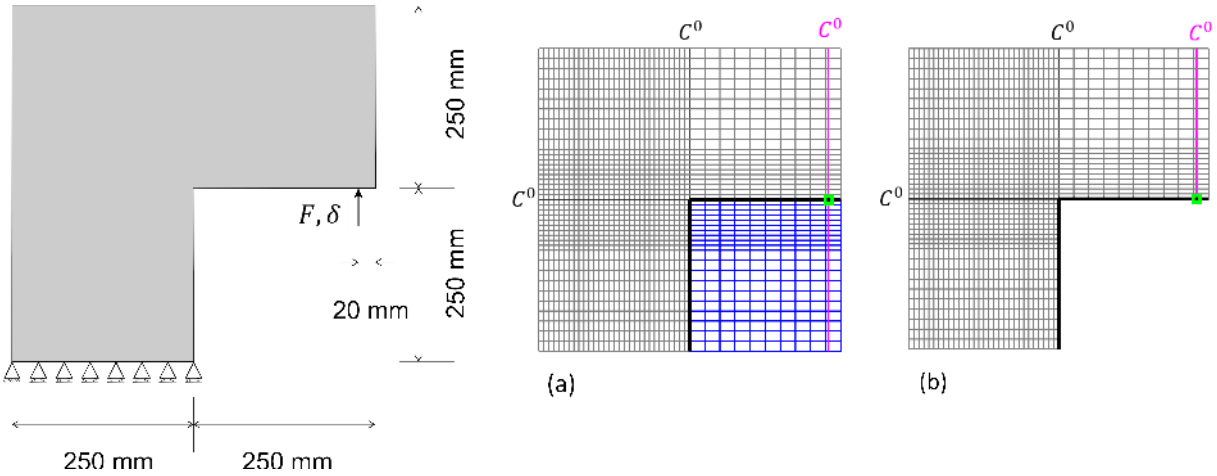

FIGURE 23 Geometry and descretisation of the L-shaped beam: (a) exploiting void level set to form the geometry, (b) final geometry after element removal. The magenta C^0 line is added to pinpoint the load location. Black lines have been added to align the mesh with the void.

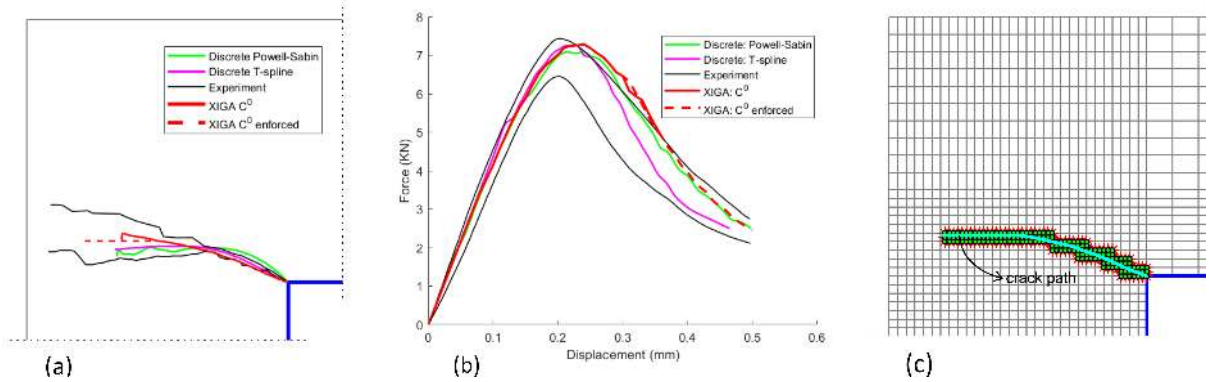

FIGURE 24 Results for L-shaped beam: (a) crack propagation profile, (b) mechanical behaviour and (c) enrichment for the XIGA C^0 enforced case. XIGA C^0 here denotes quadratic^0 − quadratic^0 interpolation.

How to cite this article: Fathi F., Chen L., and de Borst R. (2019), Extended isogeometric analysis for cohesive fracture, *Int J Numer Methods Eng., 2019;00:1–28.*

APPENDIX

A DERIVATIVES OF BÉZIER EXTRACTION BASED NURBS BASIS FUNCTION

The first derivative of the Bernstein basis function is:

$$\frac{\partial B_{k,p}(\xi)}{\partial \xi} = \frac{1}{2} p \left\{ B_{k-1,p-1}(\xi) + B_{k,p-1}(\xi) \right\} \tag{A1}$$

and the second derivative reads:

$$\frac{\partial^2 B_{k,p}(\xi)}{\partial \xi^2} = \frac{1}{4} p(p-1) \left\{ B_{k-2,p-2}(\xi) - 2B_{k-1,p-2}(\xi) + B_{k,p-2}(\xi) \right\} \tag{A2}$$

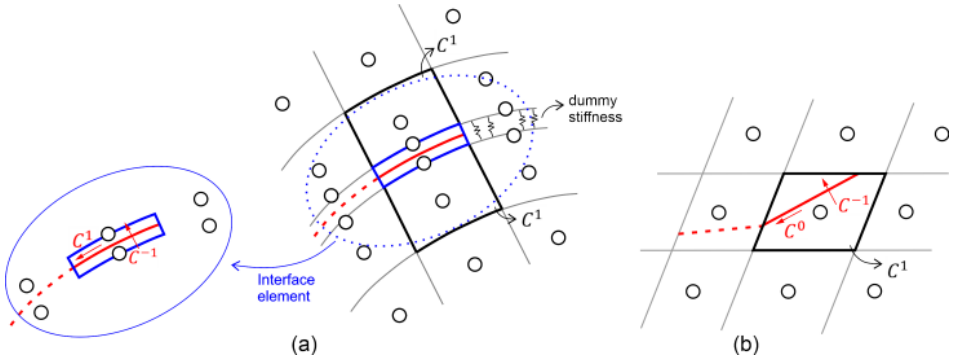

FIGURE 25 Effect of the order of continuity at element boundaries on the crack propagation direction: (a) C^1 continuity along the crack path for a discrete method with a smoother change than (b) C^0 continuity along the crack path of XIGA. A quadratic interpolation is used for both methods for the sake of comparison.

The bivariate Bernstein basis function can be defined as the tensor product of two univariate basis functions:

$$B_{k,l}^{p,q}(\xi,\eta) = B_{k,p}(\xi) \otimes B_{l,q}(\eta). \tag{A3a}$$

$$\frac{\partial B_{k,l}^{p,q}(\xi,\eta)}{\partial \xi} = \frac{1}{2} p \left\{ B_{k-1,p-1}(\xi) + B_{k,p-1}(\xi) \right\} \otimes B_{l,q}(\eta) \tag{A3b}$$

$$\frac{\partial B_{k,l}^{p,q}(\xi,\eta)}{\partial \eta} = \frac{1}{2} q B_{k,p}(\xi) \otimes \left\{ B_{l-1,q-1}(\eta) + B_{l,q-1}(\eta) \right\} \tag{A3c}$$

$$\frac{\partial^2 B_{k,l}^{p,q}(\xi,\eta)}{\partial \xi^2} = \frac{1}{4} p(p-1) \left\{ B_{k-2,p-2}(\xi) - 2B_{k-1,p-2}(\xi) + B_{k,p-2}(\xi) \right\} \otimes B_{l,q}(\eta) \tag{A3d}$$

$$\frac{\partial^2 B_{k,l}^{p,q}(\xi,\eta)}{\partial \eta^2} = \frac{1}{4} q(q-1) B_{k,p}(\xi) \otimes \left\{ B_{l-2,q-2}(\eta) - 2B_{l-1,q-2}(\eta) + B_{l,q-2}(\eta) \right\} \tag{A3e}$$

$$\frac{\partial^2 B_{k,l}^{p,q}(\xi,\eta)}{\partial \xi \partial \eta} = \frac{\partial^2 B_{k,l}^{p,q}(\xi,\eta)}{\partial \eta \partial \xi} = \frac{1}{4} pq \left\{ B_{k-1,p-1}(\xi) + B_{k,p-1}(\xi) \right\} \otimes \left\{ B_{l-1,q-1}(\eta) + B_{l,q-1}(\eta) \right\} \tag{A3f}$$

Next, the derivatives of the weighted function in Equation (30) are taken:

$$\frac{\partial W^b(\boldsymbol{\xi})}{\partial \xi_i} = \mathbf{w}^e \mathbf{C}^e \frac{\partial \boldsymbol{B}^e(\boldsymbol{\xi})}{\partial \xi_i} \tag{A4a}$$

$$\frac{\partial^2 W^b(\boldsymbol{\xi})}{\partial \xi_i \partial \xi_j} = \mathbf{w}^e \mathbf{C}^e \frac{\partial^2 \boldsymbol{B}^e(\boldsymbol{\xi})}{\partial \xi_i \partial \xi_j} \tag{A4b}$$

where $\boldsymbol{\xi} = \{\xi_1, \xi_2, \cdots\} = \{\xi, \eta, \cdots\}$ and $i, j = 1, 2, \cdots, n_{dim}$. n_{dim} is the number of dimensions, two for a bivariate NURBS. Finally, the derivatives of the bivariate Bézier-based NURBS basis function read:

$$\frac{\partial \mathbf{R}^e(\boldsymbol{\xi})}{\partial \xi_i} = \mathbf{W}^e \mathbf{C}^e \left(\frac{1}{W^b(\boldsymbol{\xi})} \frac{\partial \boldsymbol{B}^e(\boldsymbol{\xi})}{\partial \xi_i} - \frac{\partial W^b(\boldsymbol{\xi})}{\partial \xi_i} \frac{\boldsymbol{B}^e(\boldsymbol{\xi})}{\left(W^b(\boldsymbol{\xi})\right)^2} \right). \tag{A5a}$$

$$\begin{aligned} \frac{\partial^2 \mathbf{R}^e(\boldsymbol{\xi})}{\partial \xi_i \partial \xi_j} = \mathbf{W}^e \mathbf{C}^e \Bigg(& \frac{1}{W^b(\boldsymbol{\xi})} \frac{\partial^2 \boldsymbol{B}^e(\boldsymbol{\xi})}{\partial \xi_i \xi_j} - \frac{1}{\left(W^b(\boldsymbol{\xi})\right)^2} \frac{\partial W^b(\boldsymbol{\xi})}{\partial \xi_j} \frac{\partial \boldsymbol{B}^e(\boldsymbol{\xi})}{\partial \xi_i} - \frac{1}{\left(W^b(\boldsymbol{\xi})\right)^2} \frac{\partial W^b(\boldsymbol{\xi})}{\partial \xi_i} \frac{\partial \boldsymbol{B}^e(\boldsymbol{\xi})}{\partial \xi_j} \\ & - \frac{\partial^2 W^b(\boldsymbol{\xi})}{\partial \xi_i \partial \xi_j} \frac{\boldsymbol{B}^e(\boldsymbol{\xi})}{\left(W^b(\boldsymbol{\xi})\right)^2} + 2 \frac{\partial W^b(\boldsymbol{\xi})}{\partial \xi_j} \frac{\partial W^b(\boldsymbol{\xi})}{\partial \xi_i} \frac{\boldsymbol{B}^e(\boldsymbol{\xi})}{\left(W^b(\boldsymbol{\xi})\right)^3} \Bigg) \end{aligned} \tag{A5b}$$

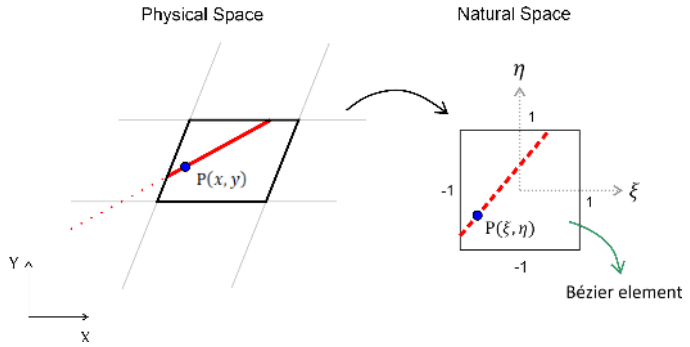

FIGURE B1 Finding ξ and η which correspond to the known physical point P(x, y) along the crack.

B POINT PROJECTION NEWTON-RAPHSON ALGORITHM

Herein, we present the point projection algorithm.

(1) Define the curve in terms of natural coordinates $C(\xi,\eta) = \sum_{i=1}^{n} R_i(\xi,\eta)X_i$ where n and X are the number and location of control points for an element, respectively, and R is the basis function of a NURBS.

(2) Define the residual $r(\xi,\eta) = C(\xi,\eta) - P(x,y)$, see Fig. B1.

(3) Solve $J_j\delta_j = \kappa_j$

$$J_j = \begin{bmatrix} f_{,\xi} & f_{,\eta} \\ g_{,\xi} & g_{,\eta} \end{bmatrix} = \begin{bmatrix} |C_{,\xi}|^2 + r\cdot C_{,\xi\xi} & C_{,\xi}\cdot C_{,\eta} + r\cdot C_{,\xi\eta} \\ C_{,\xi}\cdot C_{,\eta} + r\cdot C_{,\xi\eta} & |C_{,\eta}|^2 + r\cdot C_{,\eta\eta} \end{bmatrix}$$

$$\delta_j = \begin{bmatrix} \Delta\xi \\ \Delta\eta \end{bmatrix} = \begin{bmatrix} \xi_{j+1} - \xi_j \\ \eta_{j+1} - \eta_j \end{bmatrix}$$

$$\kappa_j = -\begin{bmatrix} f(\xi_j,\eta_j) \\ g(\xi_j,\eta_j) \end{bmatrix}$$

where

$$f(\xi,\eta) = r(\xi,\eta).C_{,\xi}(\xi,\eta) = \left(\sum_{i=1}^{n} R_i(\xi,\eta)X_i - P(x,y)\right)\cdot\sum_{i=1}^{n}\frac{\partial R_i(\xi,\eta)}{\partial\xi}X_i$$

$$g(\xi,\eta) = r(\xi,\eta).C_{,\eta}(\xi,\eta) = \left(\sum_{i=1}^{n} R_i(\xi,\eta)X_i - P(x,y)\right)\cdot\sum_{i=1}^{n}\frac{\partial R_i(\xi,\eta)}{\partial\eta}X_i$$

$$|C_{,\xi}|^2 + r\cdot C_{,\xi\xi} = |\sum_{i=1}^{n}\frac{\partial R_i(\xi,\eta)}{\partial\xi}X_i|^2 + \left(\sum_{i=1}^{n} R_i(\xi,\eta)X_i - P(x,y)\right)\cdot\sum_{i=1}^{n}\frac{\partial^2 R_i(\xi,\eta)}{\partial\xi^2}X_i$$

$$C_{,\xi}\cdot C_{,\eta} + r\cdot C_{,\xi\eta} = \sum_{i=1}^{n}\frac{\partial R_i(\xi,\eta)}{\partial\xi}X_i\cdot\sum_{i=1}^{n}\frac{\partial R_i(\xi,\eta)}{\partial\eta}X_i + \left(\sum_{i=1}^{n} R_i(\xi,\eta)X_i - P(x,y)\right)\cdot\sum_{i=1}^{n}\frac{\partial^2 R_i(\xi,\eta)}{\partial\xi\partial\eta}X_i$$

$$|C_{,\eta}|^2 + r \cdot C_{,\eta\eta} = |\sum_{i=1}^{n} \frac{\partial R_i(\xi,\eta)}{\partial \eta} X_i|^2 + \left(\sum_{i=1}^{n} R_i(\xi,\eta) X_i - P(x,y) \right) \cdot \sum_{i=1}^{n} \frac{\partial^2 R_i(\xi,\eta)}{\partial \eta^2} X_i$$

(4) Check the criterion for convergence:

$$res_1 = |(\Delta\xi) C_{,\xi}(\xi,\eta) + \Delta\eta) C_{,\eta}(\xi,\eta)|$$

$$res_2 = |r(\xi,\eta)|$$

$$res_3 = \frac{|C_{,\xi}(\xi,\eta) \cdot r(\xi,\eta)|}{|C_{,\xi}(\xi,\eta)||r(\xi,\eta)|}$$

$$res_4 = \frac{|C_{,\eta}(\xi,\eta) \cdot r(\xi,\eta)|}{|C_{,\xi}(\xi,\eta)||r(\xi,\eta)|}$$

IF $res_1 \leq \epsilon_1$ OR $res_2 \leq \epsilon_1$ OR $res_3 \leq \epsilon_2$ and $res_4 \leq \epsilon_2$
• ξ_j, η_j are accepted as final solution
ELSE
• Calculation continues for $j+1$ with two new criterion

IF $\xi_j < -1$
• set $\xi_j = 1 - (-1 - \xi_j)$
ELSEIF $\xi_j > 1$
• set $\xi_j = -1 + (\xi_j - 1)$
END

IF $\eta_j < -1$
• set $\eta_j = 1 - (-1 - \eta_j)$
ELSEIF $\eta_j > 1$
• set $\eta_j = -1 + (\eta_j - 1)$
END

• Return to (1)
END

References

1. Griffith AA. The phenomena of rupture and flow in solids. *Philosophical Transactions of the Royal Society of London* 1921; A221: 163–198.
2. Irwin G. Analysis of stresses and strains near the end of a crack traversing a plate. *Journal of Applied Mechanics* 1957; 24: 361–364.
3. Barenblatt GI. The mathematical theory of equilibrium cracks in brittle fracture.. *Archive of Applied Mechanics* 1962; 7: 55–129.
4. Dugdale DS. Yielding of steel sheets containing slits. *Journal of the Mechanics and Physics of Solids* 1960; 8: 100–108.
5. Hillerborg A, Modéer M, Petersson PE. Analysis of crack formation and crack growth in concrete by means of fracture mechanics and finite elements. *Cement and Concrete Research* 1976; 6: 773–781.

6. Rice JR, Simons DA. The stabilization of spreading shear faults by coupled deformation-diffusion effects in fluid-infiltrated porous materials. *Journal of Geophysical Research* 1976; 81: 5322–5334.

7. Simo JC, Oliver J, Armero F. An analysis of strong discontinuities induced by strain-softening in rate-independent inelastic solids. *Computational Mechanics* 1993; 12: 277–296.

8. de Borst R, Crisfield MA, Remmers JJC, Verhoosel CV. *Nonlinear Finite Element Analysis of Solids and Structures*. Chichester: John Wiley & Sons . 2012.

9. Schellekens JCJ, de Borst R. On the numerical integration of interface elements. *International Journal for Numerical Methods in Engineering* 1993; 36: 43–66.

10. Irzal F, Remmers JJC, Verhoosel CV, de Borst R. An isogeometric analysis Bézier interface element for mechanical and poromechanical fracture problems. *International Journal for Numerical Methods in Engineering* 2014; 97: 608–628.

11. Vignollet J, May S, de Borst R. On the numerical integration of isogeometric interface elements. *International Journal for Numerical Methods in Engineering* 2015; 102: 1773–1749.

12. Chen L, Lingen EJ, de Borst R. Adaptive hierarchical refinement of NURBS in cohesive fracture analysis. *International Journal for Numerical Methods in Engineering* 2017; 112: 2151–2173.

13. Chen L, Verhoosel CV, de Borst R. Discrete fracture analysis using locally refined T-splines. *International Journal for Numerical Methods in Engineering* 2018; 116: 117–140.

14. Chen L, de Borst R. Cohesive fracture analysis using Powell-Sabin B-splines. *International Journal for Numerical and Analytical Methods in Geomechanics* 2019; 43: 625–640.

15. Khoei AR. *Extended Finite Element Method: Theory and Applications*. Chichester: John Wiley & Sons . 2014.

16. Mohammadi S. *Extended Finite Element Method for Fracture Analysis of Structures*. Chichester: John Wiley & Sons . 2008.

17. Belytschko T, Black T. Elastic crack growth in finite elements with minimal remeshing. *International Journal for Numerical Methods in Engineering* 1999; 45: 601–620.

18. Moës N, Dolbow J, Belytschko T. A finite element method for crack growth without remeshing. *International Journal for Numerical Methods in Engineering* 1999; 46: 131–150.

19. Wells GN, Sluys LJ. A new method for modelling cohesive cracks using finite elements. *International Journal for Numerical Methods in Engineering* 2001; 50: 2667–2682.

20. Wells GN, Sluys LJ, de Borst R. Simulating the propagation of displacement discontinuities in a regularized strain-softening medium. *International Journal for Numerical Methods in Engineering* 2002; 53: 1235–1256.

21. Stazi FL, Budyn E, Chessa J, Belytschko T. An extended finite element method with higher-order elements for curved cracks. *Computational Mechanics* 2003; 31: 38–48.

22. Laborde P, Pommier J, Renard Y, Salaün M. High-order extended finite element method for cracked domains. *International Journal for Numerical Methods in Engineering* 2005; 64: 354–381.

23. Cottrell JA, Hughes TJR, Bazilevs Y. *Isogeometric Analysis*. Chichester: Wiley & Sons . 2009.

24. De Luycker E, Benson DJ, Belytschko T, Bazilevs Y, Hsu MC. X-FEM in isogeometric analysis for linear fracture mechanics. *International Journal for Numerical Methods in Engineering* 2011; 87: 541–565.

25. Ghorashi SS, Valizadeh N, Mohammadi S. Extended isogeometric analysis for simulation of stationary and propagating cracks. *International Journal for Numerical Methods in Engineering* 2012; 89: 1069–1101.

26. Singh SK, Singh IV, Bhardwaj G, Mishra BK. A Bézier extraction based XIGA approach for three-dimensional crack simulations. *Advances in Engineering Software* 2018; 125: 55–93.

27. Jirasek M. Nonlocal damage mechanics. *Revue Européenne de Génie Civil* 2007; 11: 993-1021.

28. Sanchez-Rivadeneira AG, Duarte CA. A stable generalized/eXtended FEM with discontinuous interpolants for fracture mechanics. *Computer Methods in Applied Mechanics and Engineering* 2019; 345: 876–918.

29. Zhang Q, Babuška I, Banerjee U. Robustness in stable generalized finite element methods (SGFEM) applied to Poisson problems with crack singularities. *Computer Methods in Applied Mechanics and Engineering* 2016; 311: 476–502.

30. Taylor RL, Zienkiewicz OC, Oñate E. A hierarchical finite element method based on the partition of unity. *Computer Methods in Applied Mechanics and Engineering* 1998; 152: 73–84.

31. Fries TP, Belytschko T. The extended/generalized finite element method: an overview of the method and its applications. *International Journal for Numerical Methods in Engineering* 2010; 84: 253–304.

32. Verhoosel CV, Scott MA, de Borst R, Hughes TJR. An isogeometric approach to cohesive zone modeling. *International Journal for Numerical Methods in Engineering* 2011; 87: 336–360.

33. Verhoosel CV, Scott MA, Hughes TJR, de Borst R. An isogeometric analysis approach to gradient damage models. *International Journal for Numerical Methods in Engineering* 2011; 86: 115–134.

34. Borden MJ, Scott MA, Evans JA, Hughes TJR. Isogeometric finite element data structures based on Bézier extraction of NURBS. *International Journal for Numerical Methods in Engineering* 2011; 87: 15–47.

35. de Borst R, Chen L. The role of Bézier extraction in adaptive isogeometric analysis: Local refinement and hierarchical refinement. *International Journal for Numerical Methods in Engineering* 2018; 113: 999–1019.

36. Fries TP. A corrected XFEM approximation without problems in blending elements. *International Journal for Numerical Methods in Engineering* 2008; 75: 503–532.

37. Piegl L, Tiller W. *The NURBS book*. Dordrecht: Springer Science & Business Media . 2012.

38. Unger JF, Eckardt S, Könke C. Modelling of cohesive crack growth in concrete structures with the extended finite element method. *Computer Methods in Applied Mechanics and Engineering* 2007; 196: 4087–4100.

39. Dumstorff P. *Modellierung und Numerische Simulation von Rissfortschritt in Spröden und Quasi-Spröden Materialien auf Basis der Extended Finite Element Method*. PhD thesis. Ruhr-Universität Bochum, Bochum; 2006.